Dissertation

submitted to the

Combined Faculty of Mathematics, Engineering and Natural Sciences

of Heidelberg University, Germany

for the degree of

Doctor of Natural Sciences

Put forward by

Zewen Sun

born in: Taiyuan City

Oral examination: 17-04-2026

Investigations on ^{208}Pb fine-structure anomaly and nuclear charge radius via muonic atom calculations

Referees: PD. Dr. Natalia S. Oreshkina

Prof. Dr. Joerg Jaeckel

Abstract

In this thesis, we theoretically investigate the ^{208}Pb nuclear charge radius and the associated fine-structure anomaly, which is a discrepancy between the experimental measurements and theoretical predictions for the muonic ^{208}Pb spectrum. By integrating state-of-the-art calculation methods for quantum electrodynamics corrections and a systematic uncertainty analysis, we perform a fit between theoretical and experimental muonic atom transition energies. This fit yields a new root-mean-square nuclear charge radius of 5.5062(5) fm for ^{208}Pb. Meanwhile, fine-structure anomaly of muonic ^{208}Pb is significantly reduced but the residual discrepancy remains larger than the predicted uncertainty. The calculation methods, including our improvement, the fitting procedure, and the uncertainty analysis are presented in details. Finally, we discuss the results and examine potential sources of the remaining anomaly.

Zusammenfassung

In dieser Arbeit untersuchen wir theoretisch den Kernladungsradius von ^{208}Pb und die damit verbundene Feinstrukturanomalie, die eine Diskrepanz zwischen experimentellen Messungen und theoretischen Vorhersagen für das myonische ^{208}Pb-Spektrum darstellt. Durch die Integration modernster Berechnungsmethoden für Quantenelektrodynamik-Korrekturen und einer systematischen Unsicherheitsanalyse führen wir einen Fit zwischen theoretischen und experimentellen Übergangsenergien im myonischen Atom durch. Dieser Fit ergibt einen neuen quadratisch gemittelten Kernladungsradius von 5,5062(5) fm für ^{208}Pb. Zugleich wird die Feinstrukturanomalie von myonischem ^{208}Pb deutlich reduziert, diese bleibt jedoch größer als die vorhergesagte Unsicherheit. Die Berechnungsmethoden, einschließlich unserer Verbesserungen, das Anpassungsverfahren und die Unsicherheitsanalyse werden im Detail vorgestellt. Abschließend diskutieren wir die Ergebnisse und erörtern mögliche Ursachen der verbleibenden Anomalie.

In the course of this thesis, the following articles have been published in peer-reviewed journals:

- Zewen Sun, Igor A. Valuev, and Natalia S. Oreshkina
  Nuclear deformation effects in the spectra of highly charged ions
  Phys. Rev. Research **6**, 023327 (2024) (Ref. [1])

- Zewen Sun, Konstantin A. Beyer, Zoia A. Mandrykina, Igor A. Valuev, Christoph H. Keitel, and Natalia S. Oreshkina
  ^{208}*Pb Nuclear Charge Radius Revisited: Closing the Fine-Structure-Anomaly Gap*
  Phys. Rev. Lett. 135, 163002 (2025) (Ref. [2])

The following articles have been submitted to peer-reviewed journals:

- Konstantin A. Beyer, Igor A. Valuev, Zoia A. Mandrykina, Zewen Sun, Natalia S. Oreshkina
  Relativistic recoil as a key to the fine-structure puzzle in muonic ^{90}*Zr*
  arXiv:2511.22298 (Ref. [3])

- Zoia A. Mandrykina, Zewen Sun, and Natalia S. Oreshkina
  Wichmann-Kroll Correction in Muonic Atoms and Hydrogen-Like Electronic Ions: a Comparative Study of Two Methods
  arXiv:2601.22979 (Ref. [4])

Contents

List of Figures

List of Tables

Chapter 1

Introduction

The advancement of physics is often propelled by the discovery of inconsistencies within established theoretical frameworks. Prior to the era of modern physics, classical theory provided a successful description of a wide range of physical phenomena. However, a series of critical experiments in the late 19th and early 20th centuries revealed fundamental limitations in classical theory, directly catalyzing the development of modern physics. For instance, in 1887, the Michelson–Morley experiment failed to detect the luminiferous aether. This indicated the problem of the Galilean transformation used in classical theory and eventually led to the discovery of the Lorentz transformation and special relativity. Similarly, the ultraviolet catastrophe in black body radiation study revealed the necessity of quantized energy. This key insight, along with other physical phenomena, e.g. the photoelectric effect, facilitated the development of quantum mechanics.

Although modern physics theory has shown remarkable success, our understanding of the physical world remains far from complete. The current frontiers of research are filled with open questions, puzzles, and inconsistencies, e.g. the unification of general relativity and quantum mechanics, building a consistent cosmological model, and the search for new particles beyond the Standard Model. Actively studying the existing problems with a continuously improving precision in both calculation and experiment is the key to the next great leap toward a more complete and robust theoretical framework.

In this thesis, we use precision calculation methods to investigate a long-standing puzzle, which is deeply connected to atomic, nuclear, and quantum electrodynamics (QED) theories. Initially pointed out by Rinker and Speth [5] in 1978, and later confirmed by Yamazaki *et al.* [6], there was a significant discrepancy between the experimental and calculation results for the energy levels of muonic ^{208}Pb. The theoretical results from these two papers were obtained by evaluating nuclear polarization

(NP) corrections, and the values were compared with the muonic atom spectroscopy measurements from Kessler *et al.* [7] and the electron scattering data from Euteneuer *et al.* [8].

In 1988, Bergem *et al.* [9] conducted the muonic ^{208}Pb spectroscopy measurement with improved precision. They also carried out the theoretical calculation as a function of ^{208}Pb nuclear charge radius and performed a fit between the experimental and theoretical data. The fit determined the best nuclear radius to maximize the agreement between the two data sets. Consequently, the resulting goodness of fit is extremely poor, revealing a persistent discrepancy. Therefore, they performed a second fit by treating the NP corrections to some states as free parameters. This is because the calculation of NP, one of the corrections to the transition energies, had large theoretical uncertainty at that time, ranging from 10% to 50%. The second fit yielded good agreement and produced a set of best-fit values for the NP corrections. However, the best-fit values showing the $2p_{1/2}$ state have a smaller NP correction than the $2p_{3/2}$, which contradicts the theoretical prediction at that time. It is believed that the discrepancy in the first fit and the anomaly in the second fit show fundamental problems of existing measurements or theoretical analysis, or could point to an undiscovered resonance excitation process of ^{208}Pb. The puzzle is known as the fine-structure anomaly of ^{208}Pb.

After several decades, better numerical methodologies have been developed, so that we can calculate NP and other corrections with improved precisions. Therefore, we theoretically reevaluate this ^{208}Pb anomaly by combining state-of-the-art numerical techniques and a systematic uncertainty analysis. In this thesis, we not only provide detailed calculation methods, but also place a particular emphasis on the nuclear model dependence of the calculations. The aim is to rigorously determine how much of the observed discrepancy can be explained within the current theoretical framework.

As a result, by combining our calculations with the measurements from Bergem *et al.* [9] via a similar fit, we significantly reduce the discrepancy. However, the discrepancy still remains larger than the estimated uncertainties, signaling a persistent problem and the necessity for further studies. The fact that the discrepancy is substantially reduced suggests that this anomaly is not likely caused by new physics beyond the Standard Model, but rather from some mechanisms within the existing theoretical framework.

Furthermore, our investigation also enables for a more precise determination of the nuclear charge radii. We report a new value for the root-mean-square charge radius of ^{208}Pb, published in Ref. [2]. The method developed here is also applied to ^{90}Zr and ^{120}Sn, as detailed in Ref. [3].

Thesis Outline

The thesis is organized in the following manner. The theoretical descriptions for all relevant calculations are presented in Chapter 2, 3, and 4, while Chapter 5 focuses on using the calculation results to investigate the ^{208}Pb fine-structure anomaly as well as the nuclear charge radius.

In Chapter 2, we demonstrate how to solve the Dirac equation to obtain the binding energies of an atom. The Dirac equation is first converted to the radial Dirac equation. Next, using rigorously derivation, we show that the radial Dirac equation for point-like nuclei can be solved analytically. Finally, various numerical techniques are introduced to solve the radial Dirac equation with finite-sized nuclear models.

In Chapter 3, we illustrate several nuclear models and their properties. Chapter 4 then covers the calculation of different energy corrections using the nuclear models introduced in Chapter 3. A particular focus is placed on the vacuum polarization correction, which includes Uehling, Wichmann-Kroll, and Källén-Sabry corrections. In particular, the Uehling contribution is further separated into electronic, muonic, and hadronic Uehling corrections.

In Chapter 5, we first provide an overview of different methods to determine the nuclear charge radius. Next, we elaborate on the muonic atom spectroscopy method while presenting some results of previous studies. Then, we discuss the ^{208}Pb fine-structure anomaly with quantitative analysis. After that, the fitting procedure and the uncertainty analysis are explained. Finally, we discuss the results and summarize the conclusions.

Units and notation

In QED calculations, two unit systems are commonly employed. The first is the Hartree atomic unit, defined by

$$e = m = \hbar = 4\pi\varepsilon_0 = 1,$$

where e is the elementary charge, m is the electron mass, $\hbar$ is the reduced Planck constant. In this unit system, the fine-structure constant α reduces to

$$\alpha = \frac{e^2}{4\pi\varepsilon_0\hbar c} = 1/c,$$

where c is the speed of light in vacuum. Therefore, the Hartree atomic unit can equivalently be specified by $c = 1/\alpha$.

The second system is the natural units, where

$$c = m = \hbar = \varepsilon_0 = 1.$$

In natural units, the fine-structure constant α becomes

$$\alpha = \frac{e^2}{4\pi\varepsilon_0\hbar c} = e^2/(4\pi).$$

Hence, the natural unit is also defined as $e^2 = 4\pi\alpha$. In this thesis, the mass m can be either the electron mass or the muon mass, known as the electronic or muonic natural units. The calculations with electronic and muonic atoms are performed within their natural units. In the end, the resulting energy corrections are shown in electronvolts (eV). Consequently, there should be no ambiguity in the numerical results.

In Chapter 2, we do not follow any specific unit system. Instead, all physical constants, e.g. $\hbar$ and c, are explicitly retained in the equations. In this way, it is easy to convert the equations into any desired unit system. In Chapter 3, we demonstrate how to express the equation of potential energy in different unit systems. After that, we adopt the natural unit to present the equations.

Throughout this thesis, three-dimensional vectors are represented by bold symbols, e.g. momentum $\mathbf{p}$. Four-vectors are denoted using tensor index notation, e.g. the four-momentum is written as p^μ. Tensor contractions follow the Einstein summation convention, e.g.

$$\begin{aligned} g_{\mu\nu}p^\nu &= g_{\mu 0}p^0 + g_{\mu 1}p^1 + g_{\mu 2}p^2 + g_{\mu 3}p^3 \\ &= p_\mu, \end{aligned}$$

where p_μ is the covariance of p^μ, and $g_{\mu\nu}$ is the Minkowski metric tensor with signature $(+---)$.

Chapter 2

Relativistic theory of atoms

Although the non-relativistic Schrödinger equation provides a fundamental picture of quantized atomic energy level, it cannot account for their fine structures, e.g. the energy splitting between $2p_{1/2}$ and $2p_{3/2}$ states. A complete theoretical description of it requires a fully relativistic treatment.

The Schrödinger equation can be viewed as the quantization of $E = \mathbf{p}^2/(2m)$, where energy E and momentum $\mathbf{p}$ are replaced by their corresponding quantum operators. The relativistic generalization of the equation follows the same prescription, but starts from the relativistic energy–momentum relation $E^2 = \mathbf{p}^2c^2 + m^2c^4$. The resulting equation is known as the Klein-Gordon equation. Since the relation involves E^2, the Klein-Gordon equation contains a second order derivative with respect to time. This term not only introduces negative energy solutions but also leads to a probability density that is not positive definite. Historically, this was considered as a fundamental flaw of the Klein-Gordon equation during a certain period.

The Dirac equation was discovered with such a historical background as an alternative approach to this relativistic generalization. By postulating Lorentz invariance and linearity in time derivative, the resulting equation contains matrix-like variables, i.e. the Dirac matrices, and the solutions are expressed as four-component wavefunctions, known as Dirac spinors or bispinors. Since the equation describes all spin-half massive particles, the four components naturally relate to the two spin states (up and down) for both particles and antiparticles. Although the Dirac equation also introduces negative energy solutions, its associated probability density always remains positive.

It is important to note that the Klein-Gordon equation only has the interpretation problem of its probability density within the framework of quantum mechanics. In quantum field theory, wavefunctions are promoted into field operators, free from the interpretation problem. The equation provides a correct description of all spinless

particles within this framework.

In this chapter, we first show how to convert the Dirac equation from its covariant form into the Dirac Hamiltonian, where we also introduce the Dirac matrices. Since most atomic systems have spherical symmetry, it is convenient to work with a spherical coordinate. Therefore, we separate the radial Dirac equation from the complete three-dimensional Dirac equation. Then, we analytically solve the radial Dirac equation for point-like nuclei, and obtain the energies and wavefunctions. Finally, we present numerical methods for solving the radial Dirac equation with finite-sized nuclei. This includes representing the wavefunctions with basis sets, e.g. Gaussian and B-spline bases, and solving the wavefunctions with the variational method. We also introduce the dual kinetic balance approach improving the numerical calculation.

2.1 The Dirac equation

The covariant form of the Dirac equation for a fermion with charge e is

$$\gamma^\mu \left(p_\mu - eA_\mu\right)\psi - mc\psi = 0, \tag{2.1}$$

where p_μ is the four-momentum operator, defined as

$$p^\mu = i\hbar\left(\frac{1}{c}\frac{\partial}{\partial t}, -\nabla\right), \quad p_\mu = i\hbar\left(\frac{1}{c}\frac{\partial}{\partial t}, \nabla\right).$$

Therefore, using the four-gradient ∂_μ notation, the equation can also be written as

$$\gamma^\mu \left(i\hbar\partial_\mu - eA_\mu\right)\psi - mc\psi = 0. \tag{2.2}$$

Here, A^μ is the four-vector potential, defined as $A^\mu = (\Phi/c, \mathbf{A})$ and $A_\mu = (\Phi/c, -\mathbf{A})$, Φ is the electric potential, and γ^μ is a four-vector with each component being a 4×4 matrix satisfying

$$\begin{aligned} (\gamma^0)^2 &= I_4 \\ (\gamma^i)^2 &= -I_4, \text{ where } i = 1, 2, 3 \\ \gamma^\mu\gamma^\nu + \gamma^\nu\gamma^\mu &= 0, \ (\mu \neq \nu), \end{aligned}$$

where I_4 is the 4×4 identity matrix. This is the necessary condition for the Dirac equation to satisfy the Klein-Gordon equation, and it can be equivalently expressed as

$$\{\gamma^\mu, \gamma^\nu\} = 2g^{\mu\nu}, \tag{2.3}$$

where the curly braces denote anticommutator, and $g^{\mu\nu}$ is the Minkowski metric tensor with signature $(+ - --)$.

When solving relativistic atoms, we consider the fermions are experiencing a static electric field from the nucleus, and therefore $\mathbf{A} = 0$. In this case, one can expand the Dirac equation as

$$\gamma^0 \left(i\hbar \frac{1}{c} \frac{\partial}{\partial t} - \frac{1}{c} V \right) \psi + i\hbar \boldsymbol{\gamma} \cdot \nabla \psi - mc\psi = 0, \tag{2.4}$$

where $V = e\Phi$ is the electric potential energy. The Dirac equation, which is more familiar to us, is presented in terms of $\boldsymbol{\alpha}$ and β matrices defined as

$$\beta \equiv \gamma^0, \ \alpha_i \equiv \beta \gamma^i, \tag{2.5}$$

also known as the Dirac matrices. Multiply both sides of the equation by β and c

$$\beta^2 \left(i\hbar \frac{\partial}{\partial t} - V \right) \psi + i\hbar c \, \boldsymbol{\alpha} \cdot \nabla \psi - \beta mc^2 \psi = 0. \tag{2.6}$$

Since $\beta^2 = I_4$, rearrange the equation, and one has

$$-i\hbar c \, \boldsymbol{\alpha} \cdot \nabla \psi + \beta mc^2 \psi + V\psi = i\hbar \frac{\partial}{\partial t} \psi. \tag{2.7}$$

Since $\mathbf{p} = -i\hbar\nabla$, the equation becomes

$$\left(c \, \boldsymbol{\alpha} \cdot \mathbf{p} + \beta mc^2 + V \right) \psi = i\hbar \frac{\partial}{\partial t} \psi. \tag{2.8}$$

We can observe that the Hamiltonian for the Dirac equation with static electric potential is

$$\boxed{H = c \, \boldsymbol{\alpha} \cdot \mathbf{p} + \beta mc^2 + V.} \tag{2.9}$$

For the Dirac matrices $\boldsymbol{\alpha}$ and β, there is more than one possible representation. Similarly to Eq. (2.3), $\boldsymbol{\alpha}$ and β must also satisfy the following conditions

$$\begin{aligned} \alpha_i^2 = \beta^2 = I_4, \\ \alpha_i \beta + \beta \alpha_i = 0, \\ \alpha_i \alpha_j + \alpha_j \alpha_i = 2\delta_{ij}. \end{aligned}$$

For H to be Hermitian, $\boldsymbol{\alpha}$ and β must be Hermitian

$$\alpha_i = \alpha_i^\dagger \text{ and } \beta = \beta^\dagger.$$

There are 4 conditions for $\boldsymbol{\alpha}$ and β in total. One of the common choices $\boldsymbol{\alpha}$ and β matrices is the Dirac representation, given by

$$\alpha_i = \begin{pmatrix} 0 & \sigma_i \\ \sigma_i & 0 \end{pmatrix}, \quad \beta = \begin{pmatrix} I & 0 \\ 0 & -I \end{pmatrix}, \tag{2.10}$$

where σ_i refer to the Pauli matrices, and $i = x, \, y, \, z$.

2.2 The radial Dirac equation

The Dirac equation, i.e. Eq. (2.9), is defined on a three-dimensional space, making it difficult to solve. However, the spherical symmetry of the nuclei allows us to define the electric potential energy $V(r)$ in the one-dimensional radial direction. Therefore, it is much easier to work with spherical coordinates. In this section, we will try to convert the Dirac equation into spherical coordinates and find an expression for the radial Dirac equation. We will find that only the radial part of the wavefunctions depends on $V(r)$, and the eigenvalues of the energies are only associated with the radial wavefunctions.

Before converting the Dirac equation into spherical coordinates, we first need to find an expression for the radial component of the momentum operator, denoted p_r. Note that

$$\mathbf{p} = -i\hbar\nabla,$$

and

$$\nabla \cdot \mathbf{v} = \frac{1}{r^2}\frac{\partial}{\partial r}\left(r^2 v_r\right) + \frac{1}{r\sin\theta}\frac{\partial}{\partial\theta}\left(\sin\theta\, v_\theta\right) + \frac{1}{r\sin\theta}\frac{\partial v_\phi}{\partial\phi},$$

where v_r, v_θ, and v_ϕ are the three components of the vector $\mathbf{v}$ in spherical coordinates. We can verify that both $(\hat{r}\cdot\mathbf{p})$ and $(\mathbf{p}\cdot\hat{r})$ are not Hermitian, as

$$\hat{r}\cdot\mathbf{p} = -i\hbar\frac{\partial}{\partial r} \tag{2.11}$$

$$\mathbf{p}\cdot\hat{r} = -i\hbar\left(\frac{\partial}{\partial r} + \frac{2}{r}\right). \tag{2.12}$$

Therefore, in order to have a Hermitian p_r, we can define it as

$$p_r = \frac{1}{2}\left(\hat{r}\cdot\mathbf{p} + \mathbf{p}\cdot\hat{r}\right) = -i\hbar\left(\frac{\partial}{\partial r} + \frac{1}{r}\right) = -i\hbar\frac{1}{r}\frac{\partial}{\partial r}\big(r(\quad)\big). \tag{2.13}$$

In the next step, we need to find an expression for $(\boldsymbol{\alpha}\cdot\mathbf{p})$ in spherical coordinates. We will expand $(\boldsymbol{\alpha}\cdot\mathbf{r})(\boldsymbol{\alpha}\cdot\mathbf{r})(\boldsymbol{\alpha}\cdot\mathbf{p})$ in two different ways and combine the two resulting expressions, in order to derive the expression for $(\boldsymbol{\alpha}\cdot\mathbf{p})$. By expanding the first two parentheses, we have

$$\begin{aligned}
&(\boldsymbol{\alpha}\cdot\mathbf{r})(\boldsymbol{\alpha}\cdot\mathbf{r})(\boldsymbol{\alpha}\cdot\mathbf{p}) \\
=&(x\alpha_x + y\alpha_y + z\alpha_z)(x\alpha_x + y\alpha_y + z\alpha_z)(\boldsymbol{\alpha}\cdot\mathbf{p}) \\
=&(x^2 + y^2 + z^2 + xy\alpha_x\alpha_y + xz\alpha_x\alpha_z + yx\alpha_y\alpha_x \\
&+ yz\alpha_y\alpha_z + zx\alpha_z\alpha_x + zy\alpha_z\alpha_y)(\boldsymbol{\alpha}\cdot\mathbf{p}) \\
=&(x^2 + y^2 + z^2)(\boldsymbol{\alpha}\cdot\mathbf{p}) \\
=&\, r^2(\boldsymbol{\alpha}\cdot\mathbf{p}).
\end{aligned} \tag{2.14}$$

In the second equality of the equation, we use $\alpha_x^2 = \alpha_y^2 = \alpha_z^2 = I_4$ to simplify the expression. In the third equality of the equation, we use the anticomutation relation of alpha matrices to cancel multiple terms. By expanding the last two parentheses, we have

$$\begin{aligned}
&(\boldsymbol{\alpha}\cdot\mathbf{r})(\boldsymbol{\alpha}\cdot\mathbf{r})(\boldsymbol{\alpha}\cdot\mathbf{p}) \\
=&(\boldsymbol{\alpha}\cdot\mathbf{r})(x\alpha_x + y\alpha_y + z\alpha_z)(\alpha_x p_x + \alpha_y p_y + \alpha_z p_z) \\
=&(\boldsymbol{\alpha}\cdot\mathbf{r})(xp_x + yp_y + zp_z + x\alpha_x\alpha_y p_y + x\alpha_x\alpha_z p_z \\
&+ y\alpha_y\alpha_x p_x + y\alpha_y\alpha_z p_z + z\alpha_z\alpha_x p_x + z\alpha_z\alpha_y p_y) \\
=&(\boldsymbol{\alpha}\cdot\mathbf{r})(\mathbf{r}\cdot\mathbf{p} + x\alpha_x\alpha_y p_y + x\alpha_x\alpha_z p_z \\
&+ y\alpha_y\alpha_x p_x + y\alpha_y\alpha_z p_z + z\alpha_z\alpha_x p_x + z\alpha_z\alpha_y p_y) \\
=&(\boldsymbol{\alpha}\cdot\mathbf{r})(\mathbf{r}\cdot\mathbf{p} + \alpha_x\alpha_y(xp_y - yp_x) + \alpha_x\alpha_z(xp_z - zp_x) + \alpha_y\alpha_z(yp_z - zp_y)) \\
=&(\boldsymbol{\alpha}\cdot\mathbf{r})\big(\mathbf{r}\cdot\mathbf{p} + i\Sigma_z(xp_y - yp_x) + i\Sigma_y(xp_z - zp_x) + i\Sigma_x(yp_z - zp_y)\big) \\
=&(\boldsymbol{\alpha}\cdot\mathbf{r})\big(\mathbf{r}\cdot\mathbf{p} + i\boldsymbol{\Sigma}\cdot(\mathbf{r}\times\mathbf{p})\big).
\end{aligned} \tag{2.15}$$

In the second equality of the equation, we use $\alpha_x^2 = \alpha_y^2 = \alpha_z^2 = I_4$ to simplify the expression. In the fourth equality of the equation, we use the anticomutation relation of the alpha matrices to simplify the expression. In the fifth equality of the equation, we introduce relativistic spin $\boldsymbol{\Sigma}$ matrices, which are defined in the following.

Combining Eqs. (2.14) and (2.15), we have

$$\begin{aligned}
r^2(\boldsymbol{\alpha}\cdot\mathbf{p}) &= (\boldsymbol{\alpha}\cdot\mathbf{r})\big(\mathbf{r}\cdot\mathbf{p} + i\boldsymbol{\Sigma}\cdot(\mathbf{r}\times\mathbf{p})\big) \\
(\boldsymbol{\alpha}\cdot\mathbf{p}) &= \frac{\boldsymbol{\alpha}\cdot\mathbf{r}}{r}\left(\frac{\mathbf{r}\cdot\mathbf{p}}{r} + \frac{i}{r}\boldsymbol{\Sigma}\cdot(\mathbf{r}\times\mathbf{p})\right) \\
(\boldsymbol{\alpha}\cdot\mathbf{p}) &= \alpha_r\left(\hat{r}\cdot\mathbf{p} + \frac{i}{r}\boldsymbol{\Sigma}\cdot(\mathbf{r}\times\mathbf{p})\right).
\end{aligned}$$

As discussed previously, the radial component of the momentum operator is defined as $p_r = (\hat{r}\cdot\mathbf{p} + \mathbf{p}\cdot\hat{r})/2$. According to Eq. (2.13), we can write the equation in terms of p_r

$$\boldsymbol{\alpha}\cdot\mathbf{p} = \alpha_r\left[p_r + \frac{i}{r}\left(\boldsymbol{\Sigma}\cdot\mathbf{L} + \hbar\right)\right], \tag{2.16}$$

where $\mathbf{L} = \mathbf{r}\times\mathbf{p}$ is the angular moment operator.

Now, we need to focus on $(\boldsymbol{\Sigma}\cdot\mathbf{L} + \hbar)$, and we can use $\mathbf{J}^2 = (\mathbf{S}+\mathbf{L})^2$ to derive an expression for it.

$$\begin{aligned}
\mathbf{J}^2 &= (\mathbf{S}+\mathbf{L})^2 \\
&= \mathbf{S}^2 + 2\mathbf{S}\cdot\mathbf{L} + \mathbf{L}^2 \\
&= \frac{3}{4}\hbar^2 + \hbar\boldsymbol{\Sigma}\cdot\mathbf{L} + \mathbf{L}^2.
\end{aligned} \tag{2.17}$$

In the third equality of the equation, we use $\mathbf{S}^2 |\psi\rangle = \hbar^2 s(s+1) |\psi\rangle = 3\hbar^2/4 |\psi\rangle$ and $\mathbf{S} = (\hbar/2)\boldsymbol{\Sigma}$ to reach the expression. Therefore, we have

$$\begin{aligned} \boldsymbol{\Sigma} \cdot \mathbf{L} + \hbar &= \frac{1}{\hbar}\left(\mathbf{J}^2 - \mathbf{L}^2 + \frac{1}{4}\hbar^2\right) \\ &= \hbar\left(j(j+1) - l(l+1) + \frac{1}{4}\right) \\ &= \pm\hbar\left(j + \frac{1}{2}\right). \end{aligned} \tag{2.18}$$

In the third equality of the equation, we use $j = (l \pm 1/2)$ to simplify the expression. Now, we can define a new operator K

$$K \equiv \beta\left(\boldsymbol{\Sigma} \cdot \mathbf{L} + \hbar\right) = \begin{pmatrix} I & 0 \\ 0 & -I \end{pmatrix} \begin{pmatrix} \sigma \cdot \mathbf{L} + \hbar & 0 \\ 0 & \sigma \cdot \mathbf{L} + \hbar \end{pmatrix}. \tag{2.19}$$

This K operator has eigenvalues of $\hbar\kappa$, where

$$\kappa \equiv (-1)^{j+l+1/2}\left(j + \frac{1}{2}\right). \tag{2.20}$$

It is easy to verify that the operator K commutes with the Hamiltonian H, therefore κ is a quantum number that defines the energy eigenstates of H. The relations between κ and other quantum numbers are shown in the following table.

	$s_{1/2}$	$p_{1/2}$	$p_{3/2}$	$d_{3/2}$	$d_{5/2}$	$f_{5/2}$	$f_{7/2}$	$g_{7/2}$	$g_{9/2}$	$h_{9/2}$	$h_{11/2}$
l	0	1	1	2	2	3	3	3	3	4	4
j	1/2	1/2	3/2	3/2	5/2	5/2	7/2	7/2	9/2	9/2	11/2
κ	-1	1	-2	2	-3	3	-4	4	-5	5	-6

Table 2.1: **Correspondence between spectroscopic notation and quantum numbers.**

Finally, we arrive at the expression of $\boldsymbol{\alpha} \cdot \mathbf{p}$ in terms of the operator K,

$$\boldsymbol{\alpha} \cdot \mathbf{p} = \alpha_r\left[p_r + \frac{i}{r}\beta\beta\left(\boldsymbol{\Sigma} \cdot \mathbf{L} + \hbar\right)\right] = \alpha_r\left(p_r + \frac{i}{r}\beta K\right), \tag{2.21}$$

where we inserted $\beta^2 = I_4$ into the equation. The Dirac equation (2.9) becomes

$$\left[c\alpha_r\left(p_r + \frac{i}{r}\beta K\right) + \beta mc^2 + V(r)\right]\psi = E\psi, \tag{2.22}$$

or equivalently

$$\left(c\alpha_r p_r + i\alpha_r\beta\frac{\hbar c\kappa}{r} + \beta mc^2 + V(r)\right)\psi = E\psi, \tag{2.23}$$

where we replaced the operator K with its eigenvalue $\hbar\kappa$. Now, the left-hand side of the equation has no derivatives with respect to the angular coordinates. Therefore, we can apply the separation of variables to ψ, and write the equation only in terms of the radial part wavefunction, which reads

$$\psi = R(r)Y(\theta, \varphi). \tag{2.24}$$

After the separation of variables, the Dirac equation becomes

$$\boxed{\left(c\alpha_r p_r + i\alpha_r\beta\frac{\hbar c\kappa}{r} + \beta mc^2 + V(r)\right)R(r) = ER(r)}. \tag{2.25}$$

To solve this radial Dirac equation, we first need to specify the representation of the α_r and β matrices. There are more than one possible representation, and we will choose the representation that can make the solving as easy as possible, which is given by

$$\alpha_r = \begin{pmatrix} 0 & -iI \\ iI & 0 \end{pmatrix} \quad \beta = \begin{pmatrix} I & 0 \\ 0 & -I \end{pmatrix}. \tag{2.26}$$

We invoke the following ansatz, which is similar to the case of the nonrelativistic Schrödinger equation

$$R(r) = \frac{1}{r}\begin{pmatrix} G(r) \\ F(r) \end{pmatrix}. \tag{2.27}$$

Substituting this ansatz into the radial Dirac equation (2.25), we have

$$\left(-i\hbar c\begin{pmatrix} 0 & -iI \\ iI & 0 \end{pmatrix}\frac{1}{r}\frac{\mathrm{d}}{\mathrm{d}r}\left(r(\ \ )\right) + i\begin{pmatrix} 0 & -iI \\ iI & 0 \end{pmatrix}\beta\frac{\hbar c\kappa}{r} + \beta mc^2 + V(r)\right)\times$$
$$\frac{1}{r}\begin{pmatrix} G(r) \\ F(r) \end{pmatrix} = E\frac{1}{r}\begin{pmatrix} G(r) \\ F(r) \end{pmatrix}.$$

Expanding it, we have

$$-\hbar c\frac{\mathrm{d}F}{\mathrm{d}r} - \frac{\hbar c\kappa}{r}F + mc^2G + VG - EG = 0$$
$$\hbar c\frac{\mathrm{d}G}{\mathrm{d}r} - \frac{\hbar c\kappa}{r}G - mc^2F + VF - EF = 0,$$

and finally, we can write the radial Dirac equation as

$$\boxed{\begin{aligned} \left(E - mc^2 - V\right)G + \hbar c\frac{\mathrm{d}F}{\mathrm{d}r} + \frac{\hbar c\kappa}{r}F = 0 \\ \left(E + mc^2 - V\right)F - \hbar c\frac{\mathrm{d}G}{\mathrm{d}r} + \frac{\hbar c\kappa}{r}G = 0. \end{aligned}} \tag{2.28}$$

This equation can be written in terms of a matrix form given by

$$\begin{pmatrix} V(r) + mc^2 & \hbar c\left(\frac{\kappa}{r} - \frac{\mathrm{d}}{\mathrm{d}r}\right) \\ \hbar c\left(\frac{\kappa}{r} + \frac{\mathrm{d}}{\mathrm{d}r}\right) & V(r) - mc^2 \end{pmatrix}\begin{pmatrix} G(r) \\ F(r) \end{pmatrix} = E\begin{pmatrix} G(r) \\ F(r) \end{pmatrix}. \tag{2.29}$$

The matrix on the right-hand side of the equation is extremely useful, since the radial wavefunctions and eigenvalues of energies can be derived or calculated using this matrix. We will denote this radial Hamiltonian matrix as H for the rest of the thesis. However, it is important to note that this H is different from the Dirac Hamiltonian matrix. More specifically, the eigenvectors of H are not the complete wavefunction, as it lack both the the $1/r$ term in Eq. (2.27) and the angular components specified in Eq. (2.24).

In the next sections, we will try to derive analytic solutions of Eq. (2.28) for point-like nuclei. Then, we will try to use numerical methods to construct the H matrix in Eq. (2.29), and obtain the numerical solution by diagonalizing H.

2.3 Solving Dirac equation in Coulomb field

The Dirac equation has analytic solutions if the nucleus can be treated as a point charge, such that the potential energy is given by

$$V(r) = -\hbar c \frac{Z\alpha}{r}, \tag{2.30}$$

where α is the fine-structure constant. This problem is known as solving the Dirac equation in the Coulomb field. To solve this problem, we will first find the asymptotic behavior of the general solution at $r \to 0$ and $r \to \infty$. Based on this, we will try to construct the general solution and solve it using the Frobenius method.

For the asymptotic solution at $r \to \infty$, Eq. (2.28) becomes

$$\left.\begin{aligned} \left(E - mc^2\right) G + \hbar c \frac{dF}{dr} = 0 \quad &\Rightarrow \quad G = \frac{\hbar c}{mc^2 - E} \frac{\partial F}{\partial r} \\ \left(E + mc^2\right) F - \hbar c \frac{dG}{dr} = 0 \quad &\Rightarrow \quad F = \frac{\hbar c}{E + mc^2} \frac{\partial G}{\partial r} \end{aligned}\right\} \begin{aligned} \frac{d^2G}{dr^2} &= \frac{m^2c^4 - E^2}{\hbar^2 c^2} G \\ \frac{d^2F}{dr^2} &= \frac{m^2c^4 - E^2}{\hbar^2 c^2} F. \end{aligned}$$

The general solution to this equation is

$$F = G = Ae^{-\rho} + Be^{+\rho}, \ \rho \equiv \frac{\sqrt{m^2c^4 - E^2}}{\hbar c} r. \tag{2.31}$$

Since the second term of the general solution is not normalizable, $B = 0$, and it yields

$$F \propto G \propto e^{-\rho}, \text{ for large } r. \tag{2.32}$$

Based on the asymptotic behavior, we claim the following ansatz to the general solution,

$$F(\rho) = f(\rho)e^{-\rho}, \quad G(\rho) = g(\rho)e^{-\rho}, \tag{2.33}$$

where $F(\rho)$ and $G(\rho)$ are two functions that need to be solved. Now in terms of $F(\rho)$ and $G(\rho)$, Eq. (2.28) becomes

$$\begin{aligned}\frac{dF}{d\rho}+\frac{\kappa F}{\rho}-\left(\sqrt{\frac{mc^2-E}{mc^2+E}}-\frac{Z\alpha}{\rho}\right)G=0\\ \frac{dG}{d\rho}-\frac{\kappa G}{\rho}-\left(\sqrt{\frac{mc^2+E}{mc^2-E}}+\frac{Z\alpha}{\rho}\right)F=0,\end{aligned} \tag{2.34}$$

and in terms of $f(\rho)$ and $g(\rho)$, we have

$$\begin{aligned}\left(\frac{d}{d\rho}-1+\frac{\kappa}{\rho}\right)f-\left(\sqrt{\frac{mc^2-E}{mc^2+E}}-\frac{Z\alpha}{\rho}\right)g=0\\ \left(\frac{d}{d\rho}-1-\frac{\kappa}{\rho}\right)g-\left(\sqrt{\frac{mc^2+E}{mc^2-E}}+\frac{Z\alpha}{\rho}\right)f=0.\end{aligned} \tag{2.35}$$

This equation is still difficult to solve, therefore, we first study the asymptotic solution at $r\to 0$, which reads

$$\left.\begin{aligned}\left(\frac{d}{d\rho}+\frac{\kappa}{\rho}\right)f+\frac{Z\alpha}{\rho}g=0\\ \left(\frac{d}{d\rho}-\frac{\kappa}{\rho}\right)g-\frac{Z\alpha}{\rho}f=0\end{aligned}\right\}\Rightarrow\begin{aligned}\left(\rho\frac{d^2}{d\rho^2}+\frac{d}{d\rho}-\frac{\kappa^2-Z^2\alpha^2}{\rho}\right)g=0\\ \left(\rho\frac{d^2}{d\rho^2}+\frac{d}{d\rho}-\frac{\kappa^2-Z^2\alpha^2}{\rho}\right)f=0.\end{aligned}$$

The general solution of it is

$$f=g=A\rho^{+\gamma}+B\rho^{-\gamma},\quad \gamma\equiv\sqrt{\kappa^2-Z^2\alpha^2}. \tag{2.36}$$

Since the second term of the general solution is not normalizable, $B=0$, such that

$$f\propto g\propto\rho^{+\gamma},\ \text{for small } r. \tag{2.37}$$

Now, we have obtained the asymptotic behavior of the solution in both small and large r. Therefore, we assume that the solution takes the following form,

$$\begin{aligned}F(\rho)\propto\rho^{\gamma}e^{-\rho}\left(\sum_{a=0}^{\infty}f_a\rho^a\right),\quad G(\rho)\propto\rho^{\gamma}e^{-\rho}\left(\sum_{a=0}^{\infty}g_a\rho^a\right),\\ \rho\equiv\frac{\sqrt{m^2c^4-E^2}}{\hbar c}r,\quad \gamma\equiv\sqrt{\kappa^2-Z^2\alpha^2},\end{aligned} \tag{2.38}$$

which is the product of the two asymptotic solutions multiplied with a power series, defined by coefficients f_a and g_a. We will use the Frobenius method to solve the coefficients. In terms of $f(\rho)$ and $g(\rho)$, we have

$$f=\rho^{\gamma}\sum_{a=0}^{\infty}f_a\rho^a,\quad g=\rho^{\gamma}\sum_{a=0}^{\infty}g_a\rho^a. \tag{2.39}$$

Substitute this into Eq. (2.35), we have

$$\begin{aligned}
&\sum_{a=0}^{\infty}\left[(\gamma+a+\kappa)f_a - f_{a-1} + \frac{E-mc^2}{q}g_{a-1} + Z\alpha g_a\right]\rho^{\gamma+a-1} = 0\\
&\sum_{a=0}^{\infty}\left[(\gamma+a-\kappa)g_a - g_{a-1} - \frac{E+mc^2}{q}f_{a-1} - Z\alpha f_a\right]\rho^{\gamma+a-1} = 0,\\
&\qquad\qquad\qquad\qquad\qquad\qquad\qquad\qquad\text{where } q \equiv \sqrt{m^2c^4 - E^2}.
\end{aligned} \tag{2.40}$$

If this equation is correct for any ρ, one must have

$$\begin{aligned}
(\gamma+a+\kappa)f_a - f_{a-1} + \frac{E-mc^2}{q}g_{a-1} + Z\alpha g_a = 0\\
(\gamma+a-\kappa)g_a - g_{a-1} - \frac{E+mc^2}{q}f_{a-1} - Z\alpha f_a = 0.
\end{aligned} \tag{2.41}$$

From the definition of q, we have $(E-mc^2)/q = -q/(E+mc^2)$, thus

$$\begin{aligned}
\left(E+mc^2\right)\left[(\gamma+a+\kappa)f_a - f_{a-1} + Z\alpha g_a\right] - qg_{a-1} = 0\\
q(\gamma+a-\kappa)g_a - qg_{a-1} - \left(E+mc^2\right)f_{a-1} - qZ\alpha f_a = 0.
\end{aligned}$$

Subtracting the above two equations to eliminate f_{a-1} and g_{a-1}, we obtain

$$\left[\left(E+mc^2\right)(\gamma+a+\kappa) + qZ\alpha\right]f_a + \left[\left(E+mc^2\right)Z\alpha - q(\gamma+a-\kappa)\right]g_a = 0.$$

Rearranging it, we have

$$f_a = \frac{q(\gamma+a-\kappa) - (E+mc^2)Z\alpha}{(E+mc^2)(\gamma+a+\kappa) + qZ\alpha}g_a. \tag{2.42}$$

Now, Eqs. (2.41) and (2.42) can be used to study coefficients f_a and g_a. However, this problem is still difficult to solve. Therefore, we first consider the $a \to \infty$ limit, and from Eq. (2.41) we have

$$\begin{aligned}
af_a - f_{a-1} + \frac{E-mc^2}{q}g_{a-1} + Z\alpha g_a \approx 0\\
ag_a - g_{a-1} - \frac{E+mc^2}{q}f_{a-1} - Z\alpha f_a \approx 0.
\end{aligned}$$

From Eq. (2.42), we have

$$f_a \approx \frac{q}{E+mc^2}g_a,$$

or equivalently

$$f_a \approx -\frac{E-mc^2}{q}g_a.$$

Combining the equations, we have

$$\begin{aligned}
-2f_{a-1} + \left[Z\alpha\frac{(E+mc^2)}{q} + a\right]f_a \approx 0\\
-2g_{a-1} + \left[a + Z\alpha\frac{(E+mc^2)}{q}\right]g_a \approx 0.
\end{aligned}$$

Apply the large a limit condition again, we have

$$f_a \approx \frac{2}{a} f_{a-1},\ g_a \approx \frac{2}{a} g_{a-1}, \tag{2.43}$$

and therefore,

$$f_a \approx \frac{2^a}{a!} f_0,\ g_a \approx \frac{2^a}{a!} g_0. \tag{2.44}$$

When summing the series to infinity, the solution will not be normalizable, as

$$\begin{aligned} \sum_{a=0}^{\infty} f_a \rho^a &= \sum_{a=0}^{\infty} \frac{2^a}{a!} f_0 \rho^a = f_0 \rho^{2a} \\ \sum_{a=0}^{\infty} g_a \rho^a &= \sum_{a=0}^{\infty} \frac{2^a}{a!} g_0 \rho^a = g_0 \rho^{2a}. \end{aligned} \tag{2.45}$$

It shows that both two series must terminate at some $a_{\max}$ before $a \to \infty$. Therefore, there exists a non-negative integer $a_{\max}$ such that

$$f_{a_{\max}+1} = g_{a_{\max}+1} = 0. \tag{2.46}$$

In Eq. (2.41), replacing $a \to (a_{\max} + 1)$, we have

$$\begin{aligned} f_{a_{\max}} &= \frac{E - mc^2}{q} g_{a_{\max}} \\ g_{a_{\max}} &= -\frac{E + mc^2}{q} f_{a_{\max}}, \end{aligned}$$

which implies

$$\frac{f_{a_{\max}}}{g_{a_{\max}}} = \frac{E - mc^2}{q}, \tag{2.47}$$

whereas Eq. (2.42) gives

$$\frac{f_{a_{\max}}}{g_{a_{\max}}} = \frac{q(\gamma + a_{\max} - \kappa) - (E + mc^2)\, Z\alpha}{(E + mc^2)\,(\gamma + a_{\max} + \kappa) + qZ\alpha}. \tag{2.48}$$

Equating the two equations, we can solve for the energy eigenvalues E, which gives

$$\frac{q(\gamma + a_{\max} - \kappa) - (E + mc^2)\, Z\alpha}{(E + mc^2)\,(\gamma + a_{\max} + \kappa) + qZ\alpha} = \frac{E - mc^2}{q}. \tag{2.49}$$

Rearranging it, we have

$$q(\gamma + a_{\max} - \kappa) - \left(E + mc^2\right) Z\alpha = \left[\left(E + mc^2\right)(\gamma + a_{\max} + \kappa) + qZ\alpha\right] \frac{E - mc^2}{q}.$$

Expanding all the terms, we have

$$q(\gamma + a_{\max} - \kappa) - \left(E + mc^2\right) Z\alpha = -q(\gamma + a_{\max} + \kappa) + \left(E - mc^2\right) Z\alpha.$$

By canceling the terms, the equation is simplified as

$$EZ\alpha = q(\gamma + a_{\max}).$$

Squaring both sides and substituting the definitions of q and γ, we have

$$E^2Z^2\alpha^2 = \left(m^2c^4 - E^2\right)\left(\sqrt{\kappa^2 - Z^2\alpha^2} + a_{\max}\right)^2.$$

Therefore, we have

$$E = mc^2\left[1 + \left(\frac{Z\alpha}{a_{\max} + \sqrt{\kappa^2 - Z^2\alpha^2}}\right)^2\right]^{-\frac{1}{2}}.$$

By defining the principal quantum number n

$$n \equiv a_{\max} + |\kappa|, \tag{2.50}$$

we finally have

$$\boxed{E = E_{n,\kappa} = mc^2\left[1 + \left(\frac{Z\alpha}{n - |\kappa| + \sqrt{\kappa^2 - Z^2\alpha^2}}\right)^2\right]^{-\frac{1}{2}}}. \tag{2.51}$$

This is the energy eigenvalue, which depends on the quantum numbers n and κ. However, we have not solved the wavefunctions corresponding to the eigenvalues. We will return to Eqs. (2.41) and (2.42), and from the equations, we can derive the following recurrence relations

$$f_a = \frac{P}{Q}f_{a-1} \tag{2.52}$$

$$g_a = \frac{M}{N}g_{a-1}, \tag{2.53}$$

where

$$P = 1 - \frac{\left(E^2 - m^2c^4\right)(\gamma + a - 1 + \kappa) + \left(E - mc^2\right)qZ\alpha}{q^2(\gamma + a - 1 - \kappa) - q\left(E + mc^2\right)Z\alpha} \tag{2.54}$$

$$Q = (\gamma + a + \kappa) + Z\alpha\frac{\left(E + mc^2\right)(\gamma + a + k) + qZ\alpha}{q(\gamma + a - \kappa) - \left(E + mc^2\right)Z\alpha} \tag{2.55}$$

$$M = 1 + \frac{q(\gamma + a - 1 - \kappa)\left(E + mc^2\right) - \left(E + mc^2\right)^2 Z\alpha}{q\left(E + mc^2\right)(\gamma + a - 1 + \kappa) + q^2Z\alpha} \tag{2.56}$$

$$N = (\gamma + a - \kappa) - Z\alpha\frac{q(\gamma + a - \kappa) - \left(E + mc^2\right)Z\alpha}{\left(E + mc^2\right)(\gamma + a + \kappa) + qZ\alpha}. \tag{2.57}$$

One can use Eq. (2.49) to verify that these recurrence relations ensures $f_{a_{\max}+1} = g_{a_{\max}+1} = 0$. The solutions generated by these recurrence relations can be expressed in terms of associated Laguerre polynomials $L_n^{\gamma}(r)$

$$f(\rho) = \sum_{a=0}^{\infty} f_a\rho^a = (\gamma - \kappa)2\rho L_{n-|\kappa|-1}^{2\gamma+1}(2\rho) + Z\alpha\frac{\gamma mc^2 - \kappa E}{\hbar cC}L_{n-|\kappa|}^{2\gamma-1}(2\rho)$$

$$g(\rho) = \sum_{a=0}^{\infty} g_a \rho^a = Z\alpha 2\rho L_{n-|\kappa|-1}^{2\gamma+1}(2\rho) + (\gamma - \kappa)\frac{\gamma mc^2 - \kappa E}{\hbar c C} L_{n-|\kappa|}^{2\gamma-1}(2\rho).$$

Finally, we can express the full radial wavefunction as

$$R(r) = \frac{1}{r}\begin{pmatrix} G(r) \\ F(r) \end{pmatrix}, \tag{2.58}$$

where $G(r)$ and $F(r)$ given by the following equations.

For $\kappa = -n$,

$$G(r) = A(2\rho)^{\gamma} e^{-\rho}(n + \gamma) \tag{2.59}$$

$$F(r) = A(2\rho)^{\gamma} e^{-\rho}(Z\alpha), \tag{2.60}$$

where A is the normalization factor given by

$$A = \frac{1}{\sqrt{2n(n+\gamma)}} \sqrt{\frac{C}{\gamma \Gamma(2\gamma)}}. \tag{2.61}$$

For $\kappa \neq -n$,

$$G(r) = A(2\rho)^{\gamma} e^{-\rho} \left[Z\alpha 2\rho L_{n-|\kappa|-1}^{2\gamma+1}(2\rho) + (\gamma - \kappa)\frac{\gamma mc^2 - \kappa E}{\hbar c C} L_{n-|\kappa|}^{2\gamma-1}(2\rho) \right] \tag{2.62}$$

$$F(r) = A(2\rho)^{\gamma} e^{-\rho} \left[(\gamma - \kappa) 2\rho L_{n-|\kappa|-1}^{2\gamma+1}(2\rho) + Z\alpha \frac{\gamma mc^2 - \kappa E}{\hbar c C} L_{n-|\kappa|}^{2\gamma-1}(2\rho) \right], \tag{2.63}$$

where, in this case, the normalization factor A is

$$A = \frac{1}{\sqrt{2\kappa(\kappa - \gamma)}} \sqrt{\frac{C}{n - |\kappa| + \gamma} \frac{(n - |\kappa| - 1)!}{\Gamma(n - |\kappa| + 2\gamma + 1)} \frac{1}{2} \left[\left(\frac{\kappa E}{\gamma mc^2} \right)^2 + \frac{\kappa E}{\gamma mc^2} \right]}. \tag{2.64}$$

Here, parameters γ, C, and variable ρ are defined as

$$\gamma \equiv \sqrt{\kappa^2 - Z^2\alpha^2}, \quad C \equiv \frac{\sqrt{m^2c^4 - E^2}}{\hbar c}, \quad \rho \equiv Cr, \tag{2.65}$$

and $\Gamma(x)$ is the gamma function. In addition, n and κ are quantum numbers, and E is the energy of the state.

It should be note that the above wavefunctions depends on the representation chosen for α_r and β matrices, as defined in Eq. (2.26). The Dirac representation of α_r and β matrices is a more common choice, which yields

$$R(r) = \frac{1}{r}\begin{pmatrix} G(r) \\ iF(r) \end{pmatrix}, \tag{2.66}$$

with an additional i. This difference is purely representational and does not alter any physical interpretation.

2.4 Numerical methods

We have shown that the radial Dirac equation for point-like nuclei can be solved analytically. To obtain the solutions for finite-sized nuclei, it requires numerical calculation. The following sections cover numerical approaches solving the radial Dirac equation.

2.4.1 Rayleigh–Ritz method

The wavefunctions solved from the radial Dirac equation can be regarded as vectors belonging to a vector space, i.e. the Hilbert space. We can choose a basis, a set of real-valued functions, spanning this Hilbert space, such that any wavefunction can be expressed as a linear combination of the basis functions. In principle, since the Hilbert space has infinite dimensions, an infinite number of basis functions is required. In practice, a finite set provides a good approximation, which converges to the exact result at a large number of basis functions.

As for the radial Dirac equation, the eigenvectors are bispinors, denoted as $u(r)$ here,

$$u(r) \equiv \begin{pmatrix} G(r) \\ F(r) \end{pmatrix}. \tag{2.67}$$

By defining a basis $\{u_i(r)\}$, consisting of $2N$ numbers of basis functions, any wavefunction can be written as a linear combination,

$$u(r) = \sum_{i=1}^{2N} c_i \, u_i(r) = \sum_{i=1}^{N} \begin{pmatrix} c_i \, u_i(r) \\ c_{i+N} \, u_{i+N}(r) \end{pmatrix}. \tag{2.68}$$

In this way, any wavefunction can be represented as $2N$ real coefficients. By rearranging the radial Dirac equation,

$$H \left| u \right\rangle = E \left| u \right\rangle \tag{2.69}$$

we have

$$E = \frac{\langle u | \, H \, | u \rangle}{\langle u | u \rangle} = \sum_i \sum_j \frac{c_i c_j H_{ij}}{c_i c_j C_{ij}}, \tag{2.70}$$

where $H_{ij} = \langle u_i | \, H \, | u_j \rangle$ and $C_{ij} = \langle u_i | u_j \rangle$. Now, every energy eigenvalue is also presented as the sum of coefficients.

If we take a trial wavefunction, by randomly generating coefficients $\{c_i\}$, it must have energy greater or equals to the ground state energy. By varying the coefficients, we should obtain the ground state wavefunction when the energy reaches the global minimum of the parameter space. The energy reaches local or global minimum point when

$$\frac{\partial E}{\partial c_i} = 0, \tag{2.71}$$

and derivative is given by

$$\begin{aligned}\frac{\partial E}{\partial c_i} &= \frac{\sum c_j H_{ij}}{\sum c_i c_j C_{ij}} - \frac{\sum c_i c_j H_{ij} \sum c_j C_{ij}}{\left(\sum c_i c_j C_{ij}\right)^2} \\ &= \frac{\sum c_j \left(H_{ij} - E\, C_{ij}\right)}{\sum c_i c_j C_{ij}}.\end{aligned} \tag{2.72}$$

For this derivative to be zero, we must have

$$\sum_j c_j \left(H_{ij} - E C_{ij}\right) = 0. \tag{2.73}$$

Multiplying both sides by $|u_j\rangle$, we have

$$H\,|u\rangle = E\,C\,|u\rangle\,. \tag{2.74}$$

Since H and C are matrices and E is a scalar, we identify this as a generalized eigenvalue problem. By solving this generalized eigenvalue problem, we obtain a set of energies and a corresponding set of orthogonal wavefunctions, which span the space defined by the basis. Since the basis is assumed to be complete, the lowest energies in this set must be the ground state energy. The remaining energies and their associated wavefunctions must represent the excited states of the system. This approach, solving the radial Dirac equation with a finite basis set using the variational method, constitutes the Rayleigh–Ritz method.

As for the numerical techniques, if matrix C is invertible or positive definite, the generalized eigenvalue problem can be efficiently solved using, e.g., scipy.linalg.eigh function in SciPy library in Python, or DSYGV subroutine in LAPACK library of Fortran.

2.4.2 Gaussian basis

To obtain accurate solutions, the finite basis set employed in the Rayleigh–Ritz method must sufficiently span the Hilbert space. Therefore, it is important to choose an appropriate set of basis functions. In Sec. 2.3, we demonstrate the analytic wavefunctions for point-like nuclei behave as power functions near $r \to 0$ and as exponential functions at $r \to \infty$. By considering the asymptotic forms, the Gaussian basis are constructed as

$$\pi_i^{\pm}(r) = \mathcal{N} r^{d_\pm} \exp\left(-\zeta_i r^2\right), \tag{2.75}$$

where $\mathcal{N}$ is the normalization factor, $d_\pm$ and ζ_i are positive parameters. The power function $r^{d_\pm}$ and the Gaussian term $\exp(-\zeta_i r^2)$ attempt to characterize the asymptotic behaviors of the radial wavefunctions. Labeled by $\pm$ sign, the functions $\pi_i^+(r)$ and $\pi_i^-(r)$ serve as the basis for the large and small wavefunction components, $G(r)$ and

$F(r)$, respectively. For realistic nuclear models, the charge distribution is roughly a constant at $r \to 0$, therefore the behavior of the asymptotic wavefunction is similar to that of the free particle, such that

$$d_\pm = \left|\kappa \pm \frac{1}{2}\right| + \frac{1}{2}. \tag{2.76}$$

The ζ_i coefficients must follow certain conditions for the basis functions to be sufficiently linearly independent, and we have

$$\zeta_i = \zeta_1 \left(\zeta_N/\zeta_1\right)^{\frac{i-1}{N-1}}, \tag{2.77}$$

where N is the number of functions in the basis set. In this work, the first and last coefficients, ζ_1 and ζ_N, are determined according to

$$\begin{aligned} \zeta_1 = 1/\left(2\,r_1^2\right),\ \zeta_N = 1/\left(2\,r_N^2\right) \\ r_1 = r_{\mathrm{rms}}/20,\ r_N = 100\,r_{\mathrm{B}}/Z, \end{aligned} \tag{2.78}$$

where r_{rms} is the root-mean-square (rms) nuclear charge radius, Z is the nuclear charge number, and r_{B} is the Bohr radius defined by

$$r_{\mathrm{B}} = \frac{4\pi\varepsilon_0\hbar^2}{e^2 m} = \frac{\hbar}{mc\alpha}, \tag{2.79}$$

and α is the fine-structure constant. The term r_{B}/Z approximates the most probable distance between the $1s_{1/2}$ electron and the nucleus with charge number Z. This choice of ζ_i ensures that the first basis function is located inside the nucleus, and the last basis function aims to reach the farthest distance where the electrons could be. In this manner, the basis functions cover the entire range of interest.

In addition, the first and second derivatives of Gaussian basis functions are

$$\frac{\mathrm{d}}{\mathrm{d}r}\pi_i(r) = \mathcal{N}\left(d\,r^{d-1} - 2\zeta_i\,r^{d+1}\right)\exp\left(-\zeta_i r^2\right), \tag{2.80}$$

and

$$\frac{\mathrm{d}^2}{\mathrm{d}r^2}\pi_i(r) = \mathcal{N}\left[\left(d^2 - d\right)\,r^{d-2} - \zeta_i\left(4d+2\right)\,r^d + 4\zeta_i\,r^{d+2}\right]\exp\left(-\zeta_i r^2\right). \tag{2.81}$$

To solve the radial Dirac equation using the Rayleigh–Ritz method, we need to construct the H and C matrices, defined by Eq. (2.74), under a Gaussian basis. Their matrix elements involve integrals over products of Gaussian basis functions. While these integrals can be calculated numerically, a simple and efficient analytical approach is available via using the Gamma function. Since the parameters are positive, $d, \zeta > 0$, the integral can be simplified as

$$\mathcal{G}(d,\zeta) \equiv \int_0^\infty r^d \exp\left(-\zeta r^2\right)\mathrm{d}r = \frac{1}{2}\,\zeta^{-(d+1)/2}\,\Gamma\left(\frac{d+1}{2}\right), \tag{2.82}$$

where $\Gamma(s)$ is the gamma function, and we used $\mathcal{G}(d,\zeta)$ to denote this integral. For the same integral with definite nonnegative limits, $b \geqslant a \geqslant 0$, we have

$$\begin{aligned}\mathcal{G}(d,\zeta,a) &\equiv \int_a^\infty r^d \exp\left(-\zeta r^2\right) \mathrm{d}r \\ &= \frac{1}{2}\,\zeta^{-(d+1)/2}\left[\Gamma\left(\frac{d+1}{2}\right) - \Gamma\left(\frac{d+1}{2}, a^2\zeta\right)\right], \qquad (2.83)\\ \mathcal{G}(d,\zeta,a,b) &\equiv \int_a^b r^d \exp\left(-\zeta r^2\right) \mathrm{d}r \\ &= \frac{1}{2}\,\zeta^{-(d+1)/2}\left[\Gamma\left(\frac{d+1}{2}, b^2\zeta\right) - \Gamma\left(\frac{d+1}{2}, a^2\zeta\right)\right], \qquad (2.84)\end{aligned}$$

where $\Gamma(s,x)$ is the lower incomplete gamma function defined as

$$\Gamma(s,x) = \int_0^x t^{s-1}\exp(-t)\,\mathrm{d}t. \qquad (2.85)$$

The gamma and incomplete gamma functions can easily be numerically calculated. It should be noted that different numerical libraries might define their lower incomplete gamma function differently, e.g. the SciPy library, and it is important to modify it to become Eq. (2.85).

The matrix elements of C depend solely on the chosen basis functions. Since the two components of the wavefunction are expressed separately as

$$G(r) = \sum_{i=1}^{N} c_i\,\pi_i^+(r) \qquad (2.86)$$

$$F(r) = \sum_{i=1}^{N} c_{i+N}\,\pi_i^-(r) \qquad (2.87)$$

the C matrix is block-diagonal, such that

$$C = \begin{pmatrix} C_{11} & 0 \\ 0 & C_{22} \end{pmatrix}. \qquad (2.88)$$

The matrix elements within each block are given by

$$\left\langle \pi_i^+ \right| C_{11} \left| \pi_j^+ \right\rangle = \mathcal{C}_{ij}^{++}(0) \qquad (2.89)$$

$$\left\langle \pi_i^- \right| C_{22} \left| \pi_j^- \right\rangle = \mathcal{C}_{ij}^{--}(0), \qquad (2.90)$$

where we use $\mathcal{C}_{ij}^{\pm\pm}(x)$ to denote the integrals of

$$\mathcal{C}_{ij}^{++}(x) \equiv \mathcal{G}\left(2d^+ + x, \zeta_i + \zeta_j\right) \qquad (2.91)$$

$$\mathcal{C}_{ij}^{+-}(x) \equiv \mathcal{G}\left(d^+ + d^- + x, \zeta_i + \zeta_j\right) \qquad (2.92)$$

$$\mathcal{C}_{ij}^{--}(x) \equiv \mathcal{G}\left(2d^- + x, \zeta_i + \zeta_j\right), \qquad (2.93)$$

and $\mathcal{G}(d,\zeta)$ is defined in Eq. (2.82).

Similarly, the matrix elements of H can also be evaluated using $\mathcal{C}_{ij}^{\pm\pm}(x)$. Since the radial Dirac matrix can be divided into four blocks,

$$H = \begin{pmatrix} H_{11} & H_{12} \\ H_{21} & H_{22} \end{pmatrix} = \begin{pmatrix} V(r) + mc^2 & \hbar c \left(\frac{\kappa}{r} - \frac{\mathrm{d}}{\mathrm{d}r}\right) \\ \hbar c \left(\frac{\kappa}{r} + \frac{\mathrm{d}}{\mathrm{d}r}\right) & V(r) - mc^2 \end{pmatrix}, \tag{2.94}$$

the matrix elements within each block are given by

$$\left\langle \pi_i^+ \right| H_{11} \left| \pi_j^+ \right\rangle = V_{ij}^{++} + mc^2\, \mathcal{C}_{ij}^{++}(0) \tag{2.95}$$

$$\left\langle \pi_i^+ \right| H_{12} \left| \pi_j^- \right\rangle = \hbar c\kappa\, \mathcal{C}_{ij}^{+-}(-1) - \hbar c \left[d^-\, \mathcal{C}_{ij}^{+-}(-1) - 2\zeta_j\, \mathcal{C}_{ij}^{+-}(+1) \right] \tag{2.96}$$

$$\left\langle \pi_i^+ \right| H_{21} \left| \pi_j^- \right\rangle = \hbar c\kappa\, \mathcal{C}_{ij}^{+-}(-1) + \hbar c \left[d^+\, \mathcal{C}_{ij}^{+-}(-1) - 2\zeta_j\, \mathcal{C}_{ij}^{+-}(+1) \right] \tag{2.97}$$

$$\left\langle \pi_i^- \right| H_{22} \left| \pi_j^- \right\rangle = V_{ij}^{--} - mc^2\, \mathcal{C}_{ij}^{--}(0). \tag{2.98}$$

The blocks H_{11} and H_{22} depend on the potential energy $V(r)$. The terms V_{ij}^{++} and V_{ij}^{--} are defined as

$$V_{ij}^{++} = \left\langle \pi_i^+ \right| V \left| \pi_j^+ \right\rangle \tag{2.99}$$

$$V_{ij}^{--} = \left\langle \pi_i^- \right| V \left| \pi_j^- \right\rangle, \tag{2.100}$$

and their values depends on the choice of specific nuclear model of the charge distribution. For instance, considering the simplest model, the point-like nucleus, we have

$$V_{ij}^{++} = -\hbar c Z\alpha\, \mathcal{C}_{ij}^{++}(-1) \tag{2.101}$$

$$V_{ij}^{--} = -\hbar c Z\alpha\, \mathcal{C}_{ij}^{--}(-1). \tag{2.102}$$

For other nuclear models, V_{ij}^{++} and V_{ij}^{--} are calculated using similar methods.

It is important to note that the use of a large number of Gaussian basis functions, i.e. large N, can introduce numerical difficulties. Normally, numerical floating-point arithmetic numbers take the double precision format, occupying 64 bits of computer memory. However, with this format, the Gaussian basis becomes problematic when N is too large, e.g. $N \gtrapprox 60$ in our case. At such a size, the C matrix constructed using double precision format is not positive definite. Consequently, the resulting generalized eigenvalue problem is not solvable with standard numerical techniques. This problem arises when the spatial density of basis functions is too high, and the functions come nearly linearly dependent. While smaller N avoids this issue, higher calculation accuracy often demands larger basis sets. To overcome this problem, we can extend the floating-point precision by using mpmath [10] library.

2.4.3 DKB approach

The dual kinetic balance (DKB) approach, proposed by Shabaev *et al.* [11], is a numerical method that improves the solutions of the Dirac equation constructed using finite basis sets. The DKB approach ensures that the solutions satisfy the charge conjugation symmetry. Therefore, we first introduce the charge conjugation symmetry.

Recall that the radial Dirac equation is given by

$$\begin{aligned}\left(E - mc^2 - V\right) G + \hbar c \frac{\mathrm{d}F}{\mathrm{d}r} + \frac{\hbar c \kappa}{r} F = 0 \\ \left(E + mc^2 - V\right) F - \hbar c \frac{\mathrm{d}G}{\mathrm{d}r} + \frac{\hbar c \kappa}{r} G = 0.\end{aligned}$$

If we perform the transformation $E \to -E$, $V \to -V$, $\kappa \to -\kappa$, and $G \leftrightarrow F$, the radial Dirac equation is invariant. Since changing the potential energy from $V \to -V$ is equivalent to inverting the sign of the particle charge, this symmetry is called the charge conjugation symmetry, also denoted as the $\mathcal{C}$ symmetry.

The solution of the radial Dirac equation should always satisfy the $\mathcal{C}$ symmetry. This means that an atom with an electron in the κ state should have the same magnitude of energy as an imaginary atom, which has a positron in the $-\kappa$ state, and the two energies have opposite signs. The corresponding two eigen-states of them should also be the same, but with the G and F components interchanged. However, for the numerical solutions obtained using finite basis sets, the two energies are slightly different in magnitude, which violated the $\mathcal{C}$ symmetry. Depending on the choice of basis set, the two eigen-states can also slightly violate the $\mathcal{C}$ symmetry. The detailed numerical results obtained from the Gaussian basis are presented and discussed by Salman and Saue [12].

In addition to the $\mathcal{C}$ symmetry problem, the energy spectrum obtained from a finite basis set calculation can contain spurious states, which do not correspond to any physical state. These numerical problems, arise from employing the Rayleigh–Ritz method with a finite basis set, can be effectively eliminated by adopting the DKB approach.

The key idea of DKB is to construct $G(r)$ and $F(r)$ using two interrelated bases. In the last section, $G(r)$ and $F(r)$ are represented by two separate bases with independent coefficients. However, $G(r)$ and $F(r)$ should be coupled via the operators H_{12} and H_{21} defined in Eq. (2.94). Therefore, using the Gaussian basis as an example, the DKB approach can be implemented by taking

$$u_i(r) = \begin{pmatrix} \pi_i^+ \\ \frac{\hbar}{2mc}\left(\frac{\mathrm{d}}{\mathrm{d}r} + \frac{\kappa}{r}\right)\pi_i^+ \end{pmatrix}, \tag{2.103}$$

$$u_{i+N}(r) = \begin{pmatrix} \frac{\hbar}{2mc}\left(\frac{\mathrm{d}}{\mathrm{d}r} - \frac{\kappa}{r}\right)\pi_i^- \\ \pi_i^- \end{pmatrix}. \tag{2.104}$$

In this way, $G(r)$ is expanded in terms of the upper component of both $u_i(r)$ and $u_{i+N}(r)$, and $F(r)$ is represented similarly by the lower components. This DKB method significantly complicates the construction of the H and C matrices in Eq. (2.74), which we present in detail in the next section using a B-spline basis.

2.4.4 B-spline basis

The B-spline basis is another widely used basis, consisting of a set of piecewise polynomial functions. The functions are called B-splines, which can be used to approximate any smooth function defined on an interval. To do this, the interval is divided into subintervals, on which the piecewise polynomial functions are defined. These functions are constructed so that they can be smoothly stitched together to represent the original smooth function.

We want to use B-splines to represent the radial wavefunction. Therefore, we consider a spherical cavity of sufficiently large radius of R_{cav}, which refers to the interval of $[0, R_{\mathrm{cav}}]$. This interval is divided into subintervals by a sequence of knots t_i, for $i = 1, 2, \ldots, (N+k+1)$, where N is the number of B-splines and k is the degree of the polynomials. The knots t_i must follow the conditions, given by

$$0 = t_1 = \cdots = t_{k+1} < t_{k+2} < \cdots < t_{N+1} = \cdots = t_{N+k+1} = R_{\mathrm{cav}}. \tag{2.105}$$

Each B-spline of degree k is denoted as $B_{i,k}(r)$, for $i = 1, 2, \ldots, N$. It is defined recursively from B-splines of degree $(k-1)$ by the relation

$$B_{i,k}(r) = \frac{r - t_i}{t_{i+k} - t_i} B_{i,k-1}(r) + \frac{t_{i+k+1} - r}{t_{i+k+1} - t_{i+1}} B_{i+1,k-1}(r). \tag{2.106}$$

The B-spline of the lowest degree $k = 0$ is defined as

$$B_{i,0}(t) = \begin{cases} 1, & \text{if } t_i \leqslant r < t_{i+1}, \\ 0, & \text{otherwise.} \end{cases} \tag{2.107}$$

As a result, a B-spline of degree k satisfies

$$B_{i,k}(r) = \begin{cases} \text{non-zero}, & \text{if } t_i \leq t < t_{i+k+1}, \\ 0, & \text{if } t < t_i \text{ or } t \geqslant t_{i+k+1}. \end{cases} \tag{2.108}$$

Since the definition involves $(k+1)$ number of polynomials, B-splines with degree k are also said to be of order $(k+1)$.

With the above definitions, the basis for radial wavefunctions can be expressed as

$$G(r) = \sum_{i=1}^{N} c_i\, u_i(r) = \sum_{i=1}^{N} \begin{pmatrix} c_i\, B_{i,k}(r) \\ 0 \end{pmatrix}, \tag{2.109}$$

$$F(r) = \sum_{i=1}^{N} c_{i+N}\, u_{i+N}(r) = \sum_{i=1}^{N} \begin{pmatrix} 0 \\ c_{i+N}\, B_{i,k}(r) \end{pmatrix}. \tag{2.110}$$

For this B-spline basis, both of the two wavefunction components, $G(r)$ and $F(r)$, share the same basis $\{B_{i,k}\}$. Hence, there are N basis function and $2N$ coefficients for each wavefunction. This is different from the Gaussian basis, where the two components have different bases, $\{\pi_i^+\}$ and $\{\pi_i^-\}$.

Next, we demonstrate how to integrate the DKB method with a B-spline basis, where we have

$$u_i(r) = \begin{pmatrix} B_{i,k}(r) \\ \frac{\hbar}{2mc}\left(\frac{\mathrm{d}}{\mathrm{d}r} + \frac{\kappa}{r}\right) B_{i,k}(r) \end{pmatrix}, \tag{2.111}$$

$$u_{i+N}(r) = \begin{pmatrix} \frac{\hbar}{2mc}\left(\frac{\mathrm{d}}{\mathrm{d}r} - \frac{\kappa}{r}\right) B_{i,k}(r) \\ B_{i,k}(r) \end{pmatrix}. \tag{2.112}$$

The radial wavefunctions are represented as

$$G(r) = \sum_{i=1}^{N} c_i B_{i,k}(r) + c_{i+N} \frac{\hbar}{2mc} \left[B'_{i,k}(r) - \frac{\kappa}{r} B_{i,k}(r) \right], \tag{2.113}$$

$$F(r) = \sum_{i=1}^{N} c_i \frac{\hbar}{2mc} \left[B'_{i,k}(r) + \frac{\kappa}{r} B_{i,k}(r) \right] + c_{i+N} B_{i,k}(r), \tag{2.114}$$

where $B'_{i,k}(r)$ is the derivative of $B_{i,k}(r)$ with respect to r.

By defining the following notation,

$$u_{0,i} \equiv B_{i,k}(r) \tag{2.115}$$

$$u_{+,i} \equiv \frac{\hbar}{2mc} \left(\frac{\mathrm{d}}{\mathrm{d}r} + \frac{\kappa}{r} \right) B_{i,k}(r) \tag{2.116}$$

$$u_{-,i} \equiv \frac{\hbar}{2mc} \left(\frac{\mathrm{d}}{\mathrm{d}r} - \frac{\kappa}{r} \right) B_{i,k}(r), \tag{2.117}$$

the C matrix can be expressed as

$$C = \begin{pmatrix} C_{11} & C_{12} \\ C_{21} & C_{22} \end{pmatrix}, \tag{2.118}$$

where the matrix elements are given by

$$C_{11,ij} = \langle u_{0,i} | u_{0,j} \rangle + \langle u_{+,i} | u_{+,j} \rangle \tag{2.119}$$

$$C_{12,ij} = \langle u_{0,i} | u_{-,j} \rangle + \langle u_{+,i} | u_{0,j} \rangle \tag{2.120}$$

$$C_{21,ij} = \langle u_{-,i} | u_{0,j} \rangle + \langle u_{0,i} | u_{+,j} \rangle \tag{2.121}$$

$$C_{22,ij} = \langle u_{-,i} | u_{-,j} \rangle + \langle u_{0,i} | u_{0,j} \rangle . \tag{2.122}$$

Similarly, the H matrix is

$$H = \begin{pmatrix} H_{11} & H_{12} \\ H_{21} & H_{22} \end{pmatrix} = \begin{pmatrix} V(r) + mc^2 & \hbar c \left(\frac{\kappa}{r} - \frac{\mathrm{d}}{\mathrm{d}r} \right) \\ \hbar c \left(\frac{\kappa}{r} + \frac{\mathrm{d}}{\mathrm{d}r} \right) & V(r) - mc^2 \end{pmatrix},$$

where the matrix elements are

$$H_{11,ij} = \langle u_{0,i}| \, V \, |u_{0,j}\rangle + \langle u_{+,i}| \, V \, |u_{+,j}\rangle + mc^2 C_{11,ij} \tag{2.123}$$

$$H_{12,ij} = \hbar c \left[\kappa \, \langle u_{0,i}| \, 1/r \, |u_{-,j}\rangle - \left\langle u_{0,i} \middle| u'_{-,j} \right\rangle + \kappa \, \langle u_{+,i}| \, 1/r \, |u_{0,j}\rangle - \left\langle u_{+,i} \middle| u'_{0,j} \right\rangle \right] \tag{2.124}$$

$$H_{21,ij} = \hbar c \left[\kappa \, \langle u_{-,i}| \, 1/r \, |u_{0,j}\rangle + \left\langle u_{-,i} \middle| u'_{0,j} \right\rangle + \kappa \, \langle u_{0,i}| \, 1/r \, |u_{+,j}\rangle + \left\langle u_{0,i} \middle| u'_{+,j} \right\rangle \right] \tag{2.125}$$

$$H_{22,ij} = \langle u_{-,i}| \, V \, |u_{-,j}\rangle + \langle u_{0,i}| \, V \, |u_{0,j}\rangle - mc^2 C_{22,ij}. \tag{2.126}$$

Evaluating the matrix elements requires numerical integrations involving the B-splines basis functions and their first and second derivatives. Since the functions are piecewise polynomials with finite degree, the integrations can be efficiently calculated using the Gauss–Legendre quadrature.

Chapter 3

Nuclear charge models and potentials

In the last chapter, we analytically derived the energy of an electron bounded by a point-like nucleus. The energy depends on two quantum numbers, n and the absolute value of $|\kappa|$. This predicts an energy splitting between the $2p_{1/2}$ and $2p_{3/2}$ states, which is an improvement over the Schrödinger equation. However, the $2s_{1/2}$ and $2p_{1/2}$ states, both having $n = 2$ and $|\kappa| = 1$, remain degenerate in this case. Real atoms do not possess this degeneracy, since it is broken by the finite nuclear size (FNS) effect and quantum electrodynamics (QED) corrections. The magnitude of this FNS effect depends on the specific nuclear model. Consequently, nuclear model-dependent calculations are necessary for the precise determination of atomic levels and transition energies. Therefore, we need to introduce different nuclear models in terms of their charge distributions and demonstrate how to derive their corresponding electric potentials.

In this chapter, we first derive a general expression of the nuclear potential energy calculated from an arbitrary spherical nuclear charge distribution. Next, we introduce point, shell, and sphere unclear models. These models have a simple analytic nuclear charge distribution, and we show that their potential energies can be expressed as piece-wise polynomials. Then, we discuss about the Fermi nuclear model and demonstrate that polylogarithm function can be used to simply a variety of expressions related to the Fermi model. Finally, we present the deformed Fermi model, and explain how to use this model to characterize nuclear quadrupole moment.

As for the notation, to avoid confusion, we use $\rho(\mathbf{r})$ to denote the charge distribution with a base unit of (1/volume). The volume charge density at position $\mathbf{r}$ in unit of (charge/volume) is $eZ\rho(\mathbf{r})$, where e is the elementary charge, Z is the nuclear charge number. This notation is used throughout the thesis.

3.1 Potential energy derivation

If the nuclear charge distribution has spherical symmetry, denoted by $\rho(r)$, the corresponding electric potential energy can be easily derived from Gauss's law. We first use Gauss's law to find the strength of electric field, and use the electric field to derive the expression for the potential energy. According to Gauss's law, one has

$$\oint_S \mathbf{E} \cdot \mathrm{d}\mathbf{a} = \frac{Q_{\mathrm{enc}}}{\varepsilon_0}, \tag{3.1}$$

where $\mathbf{E}$ is the electric field, Q_{enc} is the total charge enclosed by the surface S, $\mathrm{d}\mathbf{a}$ is the unit normal vector of the infinitesimal area element of the surface S, and ε_0 is the vacuum permittivity. The radial symmetry of the charge distribution ensures that, if one considers a spherical surface, the magnitude of the electric field is constant on the surface and the direction of $\mathbf{E}$ is always aligned with the normal vector $\mathbf{a}$ of the surface, such that

$$\oint_S \mathbf{E} \cdot \mathrm{d}\mathbf{a} = 4\pi E r^2 = \frac{Q_{\mathrm{enc}}}{\varepsilon_0}. \tag{3.2}$$

Therefore, we have

$$E(r) = \frac{Q_{\mathrm{enc}}}{4\pi\varepsilon_0 r^2} \tag{3.3}$$

and

$$Q_{\mathrm{enc}} = 4\pi Z e \int_0^r r'^2 \rho\left(r'\right)\, \mathrm{d}r' \tag{3.4}$$

where Z is the nuclear charge number and e is the elementary charge.

In the next step, we will use the electric field to derive electric potential and potential energy. The electric field $\mathbf{E}$ and the potential Φ are connected by

$$\Phi = -\int_{\mathcal{C}} \mathbf{E} \cdot \mathrm{d}\mathbf{l}. \tag{3.5}$$

This line integral can be integrated along an arbitrary continuous path $\mathcal{C}$. Considering the straight path along the radial direction, it can be simplified as

$$\Phi(r) = -\int_{+\infty}^{r} E(r')\,\mathrm{d}r' = \int_{r}^{+\infty} E(r')\,\mathrm{d}r'. \tag{3.6}$$

Since the zero potential is defined at $r = +\infty$, the integration limit starts from $+\infty$. The electric field depends only on the charge enclosed by a sphere, but the potential depends on all charges in the space, therefore, the potential energy of a single electron (or muon) with $-e$ charge is given by

$$V(r) = -e\,\Phi(r) = V_{\mathrm{in}}(r) + V_{\mathrm{out}}(r), \tag{3.7}$$

where $V_{\mathrm{in}}(r)$ and $V_{\mathrm{out}}(r)$ are the potential energies provided by the charge inside and outside the sphere of radius r, respectively.

For $V_{\text{in}}(r)$, the enclosed charge Q_{enc} inside the sphere of radius r is a constant along the path from $r' = r$ to $r' = +\infty$, therefore, substituting Eq. (3.3) into (3.6), we have

$$V_{\text{in}}(r) = -\frac{eQ_{\text{enc}}}{4\pi\varepsilon_0}\int_r^{+\infty}\frac{1}{r'^2}\,\mathrm{d}r' = -\frac{eQ_{\text{enc}}}{4\pi\varepsilon_0 r}.$$

Combining with Eq. (3.4), the equation becomes

$$V_{\text{in}}(r) = -\frac{Ze^2}{\varepsilon_0 r}\int_0^r r'^2\rho\left(r'\right)\,\mathrm{d}r'. \tag{3.8}$$

For $V_{\text{out}}(r)$, Q_{enc} outside the sphere of radius r is not a constant along the path. However, $V_{\text{out}}(r)$ can be considered as the sum of infinitesimal $[V_{\text{in}}(r' + \mathrm{d}r') - V_{\text{in}}(r')]$ for $r' = r$ to $r' = +\infty$. Since

$$V_{\text{in}}(r' + \mathrm{d}r') - V_{\text{in}}(r') = -\frac{Ze^2}{\varepsilon_0}r'\rho\left(r'\right)\,\mathrm{d}r', \tag{3.9}$$

we have

$$V_{\text{out}}(r) = -\frac{Ze^2}{\varepsilon_0}\int_r^{\infty} r'\rho\left(r'\right)\,\mathrm{d}r'. \tag{3.10}$$

Combining Eq. (3.8) and (3.10), the total potential energy at r is

$$V(r) = -\frac{Ze^2}{\varepsilon_0}\left[\frac{1}{r}\int_0^r r'^2\rho\left(r'\right)\,\mathrm{d}r' + \int_r^{\infty} r'\rho\left(r'\right)\,\mathrm{d}r'\right]. \tag{3.11}$$

In the Hartree atomic unit system ($e = m = \hbar = 4\pi\varepsilon_0 = 1$), this equation becomes

$$V(r) = -4\pi Z\left[\frac{1}{r}\int_0^r r'^2\rho\left(r'\right)\,\mathrm{d}r' + \int_r^{\infty} r'\rho\left(r'\right)\,\mathrm{d}r'\right]. \tag{3.12}$$

In the natural atomic unit system ($c = m = \hbar = \varepsilon_0 = 1$), the equation becomes

$$V(r) = -4\pi Z\alpha\left[\frac{1}{r}\int_0^r r'^2\rho\left(r'\right)\,\mathrm{d}r' + \int_r^{\infty} r'\rho\left(r'\right)\,\mathrm{d}r'\right], \tag{3.13}$$

where $\alpha = e^2/4\pi\varepsilon_0\hbar c$ is the fine-structure constant.

3.2 Point, shell, and sphere models

The point nuclear model is the simplest model, where the nucleus is considered as a point charge localized at $r = 0$. It can be described using the Dirac delta function $\delta(r)$

$$\rho_{\text{point}}(r) = \rho_0\,\delta(r - 0), \tag{3.14}$$

where ρ_o is the normalization factor. The corresponding electric potential energy, in natural atomic unit, is

$$V^{\text{point}}(r) = -Z\alpha\frac{1}{r}, \tag{3.15}$$

In the last chapter, we have analytically derived the energies and wavefunctions of relativistic theory of atoms corresponding to this point nuclear model. This is the model we can solutions analytically, whereas other models require numerical calculations, which is also discussed in the last chapter.

The shell model is another simple model, where all the nuclear charge is localized on the surface of a shell with radius R, and it can be described as

$$\rho_{\text{shell}}(r) = \rho_0\, \delta(r - R), \tag{3.16}$$

where ρ_o is the normalization factor. The corresponding nuclear electric potential energy is

$$V^{\text{shell}}(r) = \begin{cases} -Z\alpha/R, & r < R, \\ -Z\alpha/r, & r \geqslant R. \end{cases} \tag{3.17}$$

For this shell model, it is apparent that the root-mean-square (rms) nuclear radius is

$$r_{\text{rms}} = R. \tag{3.18}$$

Although this shell model is very simple, it provides a much better description of the nucleus compared to the point model, and this can be observed in certain quantum electrodynamics (QED) calculations.

The sphere model considers the nucleus as a homogeneously charged sphere of radius R, and the expression reads

$$\rho_{\text{sphere}}(r) = \rho_0\, \theta\,(R - r) \tag{3.19}$$

where ρ_o is the normalization factor, and $\theta(r)$ is the Heaviside step function. The corresponding potential energy is

$$V^{\text{sphere}}(r) = \begin{cases} -\frac{Z\alpha}{2R}\left(3 - \frac{r^2}{R^2}\right), & r < R, \\ -Z\alpha/r, & r \geqslant R. \end{cases} \tag{3.20}$$

For this sphere model, the rms nuclear radius is

$$r_{\text{rms}} = \sqrt{\frac{3}{5}} R. \tag{3.21}$$

This sphere model is more realistic than the point and shell models.

The three nuclear models, point, shell, and sphere model, have one common feature. Their corresponding potential energies can be expressed as piecewise polynomials, as shown in Eqs. (3.15), (3.17), and (3.20). For other more complicated nuclear models, their potential energies cannot be expressed as piecewise polynomials. This feature allows us to simplify the atomic binding energy and some QED calculations, which will be discussed in the next chapter.

3.3 Fermi nuclear charge model

Fermi nuclear charge distribution is a widely accepted theoretical model for the nuclear charge distribution, which is defined by the volume charge density $eZ\rho(r)$, where e is the elementary charge, Z is the nuclear charge number, and $\rho(r)$ is given by

$$\rho_{\mathrm{2pF}}(r) = \frac{\rho_0}{1+\exp[(r-c)/a]}, \tag{3.22}$$

where r is the radial distance from the center of the nucleus, ρ_o is the normalization factor, c and a are two characteristic parameters of the model. Therefore, this is also known as the two-parameter Fermi (2pF) model.

The normalization condition reads

$$4\pi \int_0^\infty r'^2 \rho\left(r'\right)\, \mathrm{d}r' = 1. \tag{3.23}$$

Therefore, the normalization factor ρ_o is

$$\rho_0 = \frac{1}{4\pi}\left[\int_0^\infty \frac{r'^2}{1+\exp[(r'-c)/a]}\,\mathrm{d}r'\right]^{-1} \tag{3.24}$$

$$= \frac{1}{-8\pi a^3\,\mathrm{Li}_3\left(-\exp(c/a)\right)}, \tag{3.25}$$

where $\mathrm{Li}_n(x)$ is the polylogarithm of order n.

The polylogarithm can be used to simplify the integrals of the Fermi-Dirac distribution, which satisfies

$$\int_0^\infty \frac{r^j}{1+\exp(r-x)}\,\mathrm{d}r = -\Gamma(j+1)\,\mathrm{Li}_{j+1}(-e^x), \quad (j>-1), \tag{3.26}$$

where $\Gamma(j+1)$ is the gamma function. This equation can be modified into

$$\int_0^\infty \frac{r^j}{1+\exp[(r-c)/a]}\,\mathrm{d}r = -a^3\,\Gamma(j+1)\,\mathrm{Li}_{j+1}(-\exp(c/a)), \quad (j>-1), \tag{3.27}$$

which describes the Fermi charge distribution.

With the help of polylogarithm, the root-mean-square (rms) nuclear charge radius of Fermi model can be expressed as

$$r_{\mathrm{rms}}^2 = 4\pi \int_0^\infty r'^4 \rho\left(r'\right)\, \mathrm{d}r' \tag{3.28}$$

$$= 12a^2\,\frac{\mathrm{Li}_5\left(-\exp(c/a)\right)}{\mathrm{Li}_3\left(-\exp(c/a)\right)}. \tag{3.29}$$

It should be noted that the approximate expression,

$$r_{\mathrm{rms}}^2 \approx \frac{3}{5}c^2 + \frac{7\pi^2}{5}a^2, \tag{3.30}$$

also provides a relatively accurate value of the rms radius.

Similarly, the electric potential energy of a 2pF model can also be expressed in terms of polylogarithm. In natural unit, the expression is given by

$$V^{\mathrm{2pF}}(r) = \frac{Z\alpha}{2a\,\mathrm{Li}_3(\xi_0)} \left\{ \frac{2a}{r} \left[\mathrm{Li}_3(\xi(r)) - \mathrm{Li}_3(\xi_0) \right] + \mathrm{Li}_2(\xi(r)) \right\}, \tag{3.31}$$

where we use shorthand notation of

$$\xi_0 \equiv -\exp\left(\frac{c}{a}\right), \quad \xi(r) \equiv -\exp\left(\frac{c-r}{a}\right). \tag{3.32}$$

Here, ξ_0 is a constant and $\xi(r)$ is a function.

The 2pF model can be extended to a three-parameter Fermi (3pF) model by introducing an additional model parameter. This nuclear charge distribution is given by

$$\rho_{\mathrm{3pF}}(r) = \frac{\rho_0 \left[1 + w\,(r^2/c^2)\right]}{1 + \exp[(r-c)/a]}, \tag{3.33}$$

where w is the third model parameter. For $w = 0$, this model reduces to 2pF case trivially, which corresponds to a flat charge density inside the nucleus. Negative values, $w < 0$, produce a peak at the origin $r = 0$, with a decreasing charge density towards the nuclear surface. Conversely, $w > 0$ yields a lower charge density at the origin and a mild increase toward the surface. This 3pF model with more flexibility can better match the charge density profiles obtained from electron scattering experiments. The properties of a 3pF model, derived using methods similar to the 2pF case, can likewise be expressed in terms of polylogarithm.

3.4 Deformed Fermi model

Fermi nuclear charge distribution is a radial symmetric model. This symmetry leads to a zero nuclear quadrupole moment, $Q = 0$. However, most nuclei are actually deformed from the radial symmetric distribution such that $Q \neq 0$. The deformed Fermi model is designed to study this deformation effect, which is defined as

$$\rho_{\mathrm{defF}}(r,\theta) = \rho_0 \left[1 + \exp\left(\frac{r - c[1 + \beta Y_2^0(\theta)]}{a} \right) \right]^{-1}, \tag{3.34}$$

where β is the deformation parameter, θ is the polar angle ($0 \leq \theta \leqslant \pi$), and $Y_2^0(\theta)$ is the spherical harmonics of

$$Y_{l=2}^{m=0}(\theta,\varphi) = \frac{1}{4}\sqrt{\frac{5}{\pi}} \left(3\cos^2\theta - 1\right). \tag{3.35}$$

The deformed Fermi distribution is characterized by three parameters, c, a, and β. The values of these parameters are determined so that the deformed Fermi distribution matches the nuclear radius and nuclear quadrupole moment of the real nucleus.

The equation of the root-mean-square nuclear radius reads

$$\begin{aligned} r_{\mathrm{rms}}^2 &= \iiint_{\text{all space}} \rho(r,\theta)\, r^2 \,\mathrm{d}V \\ &= 2\pi \int_{\theta=0}^{\pi} \int_{r=0}^{\infty} \rho(r,\theta)\, r^4 \sin\theta \;\mathrm{d}r\mathrm{d}\theta, \end{aligned} \tag{3.36}$$

where $\mathrm{d}V$ is the three-dimensional volume element, and the factor of 2π in the second line comes from the integration of $d\varphi$. The intrinsic quadrupole moment Q_0 is given by

$$\begin{aligned} Q_0 &= eZ \iiint_{\text{all space}} \left(3\cos^2\theta - 1\right) \rho(r,\theta)\, r^2 \,\mathrm{d}V \\ &= 2\pi eZ \int_{\theta=0}^{\pi} \int_{r=0}^{\infty} 4\sqrt{\frac{\pi}{5}} Y_2^0(\theta) \rho(r,\theta)\, r^4 \sin\theta \;\mathrm{d}r\mathrm{d}\theta. \end{aligned} \tag{3.37}$$

It is useful to have

$$Q_0 = \frac{(I+1)(2I+3)}{I(2I-1)} Q_{\mathrm{spe}}, \tag{3.38}$$

since the spectroscopic quadrupole moment Q_{spe} is the result of experimental measurements, where I is the nuclear spin quantum number.

Numerically solving the two Eqs. (3.36) and (3.37) can help us to determine two parameters of the deformed Fermi nuclear model. However, the model has three parameters. Fortunately, the value of the parameter a is roughly the same for most nuclei, since the parameter a is related to the "skin thickness" t of the nuclear charge distribution by $a = t/(4\ln 3)$. It is conventional to take $t = 2.30$ fm, thus we have

$$a = \frac{t}{4\ln 3} = 0.5234 \text{ fm}. \tag{3.39}$$

Therefore, the parameter c and β of the model can be numerically calculated by associating Eqs. (3.36) and (3.37) with r_{rms} and Q_0, the values of which we know.

It should be noted that there is a widely used approximate formula for parameter β, which is

$$\beta \approx \sqrt{\frac{\pi}{5}} \frac{Q_0}{Z\, r_{\mathrm{rms}}^2} \tag{3.40}$$

$$\approx \frac{4\pi}{5Z\, r_{\mathrm{rms}}^2} \sqrt{\frac{B(E2\uparrow)}{e^2}}, \tag{3.41}$$

where $B(E2\uparrow)$ is the abbreviation for $B(E2; 0^+ \to 2^+)$, which is the reduced electric quadrupole transition rate for the nuclear ground state to 2^+ state transition. This

transition rate can be used to determine Q_0, since we have

$$Q_0[b] = \sqrt{\frac{16\pi B(E2\uparrow)[e^2b^2]}{5e^2}}. \tag{3.42}$$

In this equation, the intrinsic quadrupole moment Q_0 is in the unit of barn (b), and the quadrupole transition rate $B(E2\uparrow)$ is in the unit of $e^2\,\mathrm{barn}^2$ ($e^2\mathrm{b}^2$).

Since some literature report $B(E2\downarrow)$ instead of $B(E2\uparrow)$, it is useful to have

$$B(E2\uparrow) = \frac{2J+1}{2J_0+1}\,B(E2\downarrow), \tag{3.43}$$

with J_0 and J being spins of the lower and upper levels, respectively. Additionally, some literature report the nuclear quadrupole transition rate in Weisskopf units (W.u.), and we can use Ref. [13] to convert the unit, which is

$$B_{\mathrm{W}}(E\lambda\downarrow) = \frac{1}{4\pi}\left(\frac{3}{\lambda+3}\right)^2 1.2^{2\lambda}A^{2\lambda/3}\;e^2\mathrm{fm}^{2\lambda}, \tag{3.44}$$

where $B_{\mathrm{W}}(E\lambda\downarrow)$ is the nuclear transition rate in Weisskopf units, and A is the atomic mass number. Therefore, for $B_{\mathrm{W}}(E2\uparrow)$ transition rate, one has

$$B_{\mathrm{W}}(E2\uparrow) = 5B_{\mathrm{W}}(E2\downarrow) = 0.297\,A^{4/3}\;e^2\mathrm{fm}^4. \tag{3.45}$$

In summary, the deformed Fermi model has three parameters, a, β, and c. We take $a = 0.5234$ fm, which is the conventionally accepted value. The above equations can convert the measured nuclear quadrupole transitions into the intrinsic quadrupole moment Q_0, and the parameter β can be approximately evaluated by Eq. (3.40) using Q_0 and r_{rms}. If we know β, the parameter c can be determined by numerically solving Eq. (3.36). Otherwise, we can numerically solve Eqs. (3.36) and (3.37) to determine β and c together.

The deformed Fermi model does not have spherical symmetry but has rotational symmetry with respect to the vertical axis. However, the nuclei in the real world do not have the preference to align in a particular direction. Therefore, the nuclei have random orientations and the electrons should experience a spherically symmetric potential over time. When calculating the nuclear potential energy, we need to convert the deformed Fermi model into a spherically symmetric model by averaging $\rho(r,\theta)$ along the θ direction

$$\rho_r(r) = \int_0^\pi \rho(r,\theta)\sin\theta\,d\theta. \tag{3.46}$$

This spherically symmetric $\rho_r(r)$ is used to calculate the potential energy, which appears in the Dirac equation.

Chapter 4

QED corrections

In previous chapters, we have presented the relativistic framework of solving the atomic energies using electric potential energies from point-like or finite-sized nuclei. By using this approach involving potential energy, we are implicitly assuming serval approximations and ignoring some small but important physical effects. Therefore, it is necessary to systematically account for additional quantum electrodynamics (QED) corrections.

In this chapter, we begin with a general description, aiming to clarify the underlying assumptions used in the earlier analysis and to identify which QED effects are required to further correct the calculations. Next, we mainly focus on presenting the detailed methods for vacuum polarization (VP) calculations. This includes evaluating different VP contributions of Uehling, Wichmann-Kroll (WK), and Källén-Sabry (KS) corrections. Uehling and KS are calculated via established approaches, which involve numerical integrations of analytically defined functions. We also note that these calculations can be simplified for specific nuclear models, i.e. point, shell, and sphere models. The simplified methods are shown in separate sections. Due to the calculation complexity, we elaborate on the WK calculations using Gaussian finite-basis-set (FBS) method and discuss the numerical techniques to further improve it. Then, we extend the methods to muonic VP, and also discuss the hadronic VP calculation. Finally, we provide an overview of the corresponding methods for SE, NP, relativistic recoil, and electron screening effect.

4.1 General description

To illustrate the underlying assumptions used in the Dirac equation with only Coulomb potential, let us first consider a simple model consisting of Sun and Earth. Since Earth has a much smaller mass than Sun, we can assume the motional state of Earth will

not change the state of Sun. In this way, the gravitational interaction energy between Earth and Sun can be approximated by a gravitational potential energy, effectively reducing the two-body system into a one-body problem.

This simple model serves as a direct analogy for the atomic system. In our previous analysis, we have assumed the lepton (electron or muon) does not change the motional or internal state of the nucleus. Therefore, by solving the Dirac equation for the binding energies, we are adopting the following assumptions:

1. The massive nucleus is always located at the origin $r = 0$.

2. The nuclear states are not interacting with the lepton.

The first assumption can be corrected by the relativistic recoil effect, while the second gives rise to nuclear polarization (NP) calculation, which describes the energy shifts caused by interactions between the lepton and nuclear states. Relativistic recoil is particularly important for light atoms, whereas NP corrections are especially prominent for heavy atoms.

Furthermore, the vacuum is not completely empty space but a dynamic media consisting of virtual particle-antiparticle pairs. These virtual particles can be polarized by the nuclear charge and then interact with the bound lepton (electron or muon). This is known as vacuum polarization (VP) effect. Additionally, the lepton itself interacts with its own electromagnetic field through the continuous emission and reabsorption of virtual photons, leading to the self-energy (SE) correction. Together, these QED effects produce measurable shifts in atomic energy levels and are essential for precision theoretical predictions.

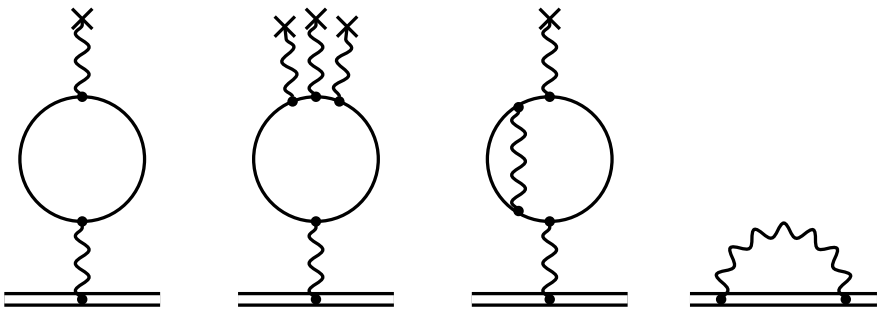

Figure 4.1: **Feynman diagrams for different QED corrections.** The double straight lines refer to the bound lepton (electron or muon).

To have a rigorous treatment, different VP contributions are calculated separately. This includes calculating Uehling, Wichmann-Kroll (WK), and Källén-Sabry (KS) corrections, whose corresponding Feynman diagrams are shown in Fig. 4.1. The Uehling

term can be further classified into the electronic and muonic Uehling corrections. To distinguish between electronic and muonic Uehling corrections for both electronic and muonic atoms, the associated Feynman diagrams are shown in Fig. 4.2.

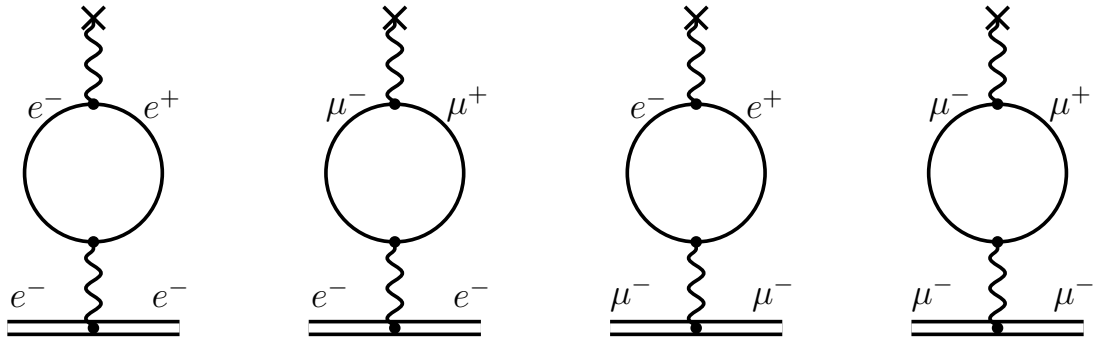

electronic Uehling for electronic atom | muonic Uehling for electronic atom | electronic Uehling for muonic atom | muonic Uehling for muonic atom

Figure 4.2: **Feynman diagrams for different types of Uehling for different atomic systems.**

It should be noted that WK and KS corrections can also be specified as electronic or muonic. However, their muonic corrections are normally negligible. Therefore, they conventionally refer to the electronic one.

4.2 Uehling correction

Uehling correction is named after Uehling [14], who found that the interaction between charged particles is not only governed by the Coulomb potential, but also an additional term associated with the electric polarization of the vacuum. It is the leading order VP correction, and also one of the largest correction for both electronic and muonic atoms. Since Uehling correction is proportional to $\alpha(Z\alpha)$ in natural unit, it corresponds to the linear term of VP with respect to nuclear charge number Z.

4.2.1 Arbitrary nuclear model

Uehling potential energy for arbitrary spherically symmetric nuclear charge distribution, $\rho(r)$, is given by

$$V_{\mathrm{Ue}}(r) = -\frac{2\alpha(Z\alpha)}{3mr}\int_0^\infty \mathrm{d}r'\, r'\rho(r')\left[\chi_2\left(2m|r-r'|\right) - \chi_2\left(2m|r+r'|\right)\right], \tag{4.1}$$

where Z is the nuclear charge number, and m is the mass of the particle. The function $\chi_2(z)$ is defined as

$$\chi_2(z) = \int_1^\infty \mathrm{d}t \exp(-tz) \frac{1}{t^2} \left(1 + \frac{1}{2t^2}\right) \sqrt{1 - \frac{1}{t^2}}. \tag{4.2}$$

To calculate Uehling potential energy for arbitrary nuclear models, it is necessary to numerically evaluate the function $\chi_2(z)$. There are different numerical methods to efficiently evaluate the function $\chi_2(z)$, and we provide a method to combine different approaches to maximize numerical efficiency and accuracy.

A numerical method provides an accurate and efficient evaluation of $\chi_2(z)$ for and only for $z \to 0$. The series expansion of $\chi_1(z)$ was derived by C. M. Sommerfeld and W. Rarita using different methods, and is introduced in Ref. [15]. McKee [16] extended the method to $\chi_2(z)$. Huang [17] elaborated it, such that

$$\chi_2(z) = E_1(z) \left(\sum_{k=0}^{\infty} z^{(2k+1)} C_{2,k} \right) + e^{-z} \left(\sum_{k=0}^{\infty} z^k D_{2,k} \right), \tag{4.3}$$

where $E_1(z)$ is the exponential integral, and coefficients $C_{2,k}$ and $D_{2,k}$ are defined as

$$C_{2,k} = \frac{(k-1)(2k-5)}{4k^2(2k+1)(k-2)} C_{2,k-1} = -\frac{b_k}{(2k+1)!} \tag{4.4}$$

$$D_{2,k} = (-1)^k \sum_{2l \geqslant k}^{\infty} \frac{(2l-k)!}{(2l+1)!} b_l, \tag{4.5}$$

where b_l follows the recurrence relation

$$b_{l+1} = \frac{l(2l-3)}{2(l^2-1)} b_l, \tag{4.6}$$

with

$$b_0 = 1,\ b_1 = 0,\ b_2 = -3/8. \tag{4.7}$$

The coefficients $C_{2,0}$ to $C_{2,7}$ and $D_{2,0}$ to $D_{2,7}$ are calculated and discussed by Huang [17]. This method can provide accurate results of $\chi_2(z)$ for $0 < z < 1$. However, since the expression contains $\sum_k z^k$, it becomes difficult to converge at large z when $z > 1$.

Klarsfeld [18] provided a numerically efficient method to calculate $\chi_2(z)$ for large z, which is given by

$$48\chi_2(z) = -\left(21z + z^3\right) K_0(z) + \left(19z^2 + z^4\right) K_1(z) + \left(27 - 18z^2 - z^4\right) Ki_1(z), \tag{4.8}$$

where $K_0(z)$ and $K_1(z)$ are modified Bessel functions of the second kind, and the function $Ki_1(z)$ is defined as

$$Ki_1(z) = \int_z^\infty dx\, K_0(x) = \int_0^{\pi/2} d\theta \exp(-z/\cos\theta). \tag{4.9}$$

For $z \geqslant 4$, $Ki_1(z)$ can be approximately evaluated using

$$\begin{aligned} Ki_1(z) = \frac{e^{-z}}{\sqrt{z}}\big[&1.253314137 - 0.195830262\,(4/z) \\ &+ 0.078937221\,(4/z)^2 - 0.050626814\,(4/z)^3 \\ &+ 0.043544223\,(4/z)^4 - 0.042846273\,(4/z)^5 \\ &+ 0.040166355\,(4/z)^6 - 0.030436033\,(4/z)^7 \\ &+ 0.016293809\,(4/z)^8 - 0.005309968\,(4/z)^9 \\ &+ 0.000781838\,(4/z)^{10}\big]. \end{aligned} \tag{4.10}$$

This approximation ensures eight significant figures of accuracy [18]. This equation is derived from the properties of Chebyshev polynomials. However, the function $Ki_1(z)$ is very difficult to approximate using any polynomial for $z \to 0$.

For $z \geqslant 1$, we can derive the following expression applying Gauss–Legendre quadrature rule to Eq. (4.9)

$$\begin{aligned} Ki_1(z) = &\left[0.3678740838^z + \left(3.363588266 \times 10^{-81}\right)^z\right] 0.01383400886 \\ &+ \left[0.3677321437^z + \left(4.465754 \times 10^{-16}\right)^z\right] 0.0318882884 \\ &+ \left[0.3670047646^z + \left(4.949679525 \times 10^{-7}\right)^z\right] 0.04922251166 \\ &+ \left(0.364934815^z + 0.0003579315395^z\right) 0.06540539989 \\ &+ \left(0.3605300373^z + 0.00639222781 7^z\right) 0.0800557289 \\ &+ \left(0.3526456149^z + 0.02882462276^z\right) 0.09282976833 \\ &+ \left(0.3400650645^z + 0.06937691747^z\right) 0.1034280148 \\ &+ \left(0.3215812948^z + 0.1203524322^z\right) 0.1116020233 \\ &+ \left(0.2960987076^z + 0.1730089477^z\right) 0.1171601896 \\ &+ \left(0.2628018488^z + 0.2214658809^z\right) 0.1199722297. \end{aligned} \tag{4.11}$$

This method ensures eight significant figures of accuracy at $z = 1$, and continues to perform better as z increases.

To conclude, it is necessary to numerically evaluate the function $\chi_2(z)$, in order to calculate Uehling potential energy for arbitrary nuclear models. For $0 < z < 1$, the function $\chi_2(z)$ can be calculated using Eq. (4.3). For $1 \leqslant z < 4$, the function $\chi_2(z)$ is calculated from the function $Ki_1(z)$, and $Ki_1(z)$ can be calculated using Eq. (4.11). For $4 \leqslant z < \infty$, the function $Ki_1(z)$ can be calculated using Eq. (4.10).

Finally, the Uehling energy correction can be calculated by including its potential energy into the Dirac equation. For point, shell, and sphere nuclear models, the Uehling calculations can be significantly simplified, which is discussed in the next section.

4.2.2 Point, shell, and sphere models

The function $\chi_2(z)$ in Eq. (4.1) belongs to a family of functions defined by

$$\chi_n(z) = \int_1^\infty dt \exp(-tz) \frac{1}{t^n} \left(1 + \frac{1}{2t^2}\right) \sqrt{1 - \frac{1}{t^2}}. \tag{4.12}$$

Based on the definition of derivative, one can show

$$\lim_{r' \to 0} \frac{\chi_2(2|r - r'|) - \chi_2(2|r + r'|)}{r'} = 4\chi_1(2r). \tag{4.13}$$

Combined with the normalization condition of nuclear charge distribution, $\int_0^\infty dr\, r^2 \rho(r) = 1/4\pi$, Uehling potential energy for a point-like nucleus becomes

$$V_{\rm Ue}^{\rm (point)}(r) = -\frac{2\alpha(Z\alpha)}{3m\pi} \frac{1}{r} \chi_1(2mr) = V_{\rm Coul}^{\rm (point)}(r) \left[\frac{2\alpha}{3m\pi} \chi_1(2mr)\right], \tag{4.14}$$

where Z is the nuclear charge number, m is mass of the particle, and $V_{\rm Coul}^{\rm (point)}(r)$ is the Coulomb potential of point-like nucleus. Analogous to Eq. (4.14), Uehling potential energy can be approximated by

$$V_{\rm Ue}(r) \approx V(r) \left[\frac{2\alpha}{3m\pi} \chi_1(2mr)\right], \tag{4.15}$$

where $V(r)$ is the electric potential of other nuclear models. However, for precision calculations, this may not be a good approximation. The function $\chi_1(z)$ can be calculated by

$$\chi_1(z) = (1 + z^2/12) K_0(z) - (5z/6 + z^3/12) K_1(z) + (3z/4 + z^3/12) Ki_1(z), \tag{4.16}$$

where $K_0(z)$ and $K_1(z)$ are modified Bessel functions of the second kind, and function $Ki_1(z)$ is defined by Eq. (4.9).

For a shell nuclear model with radius R, Uehling potential energy is given by

$$V_{\rm Ue}^{\rm (shell)}(r) = -\frac{\alpha(Z\alpha)}{6\pi m R r} \left[\chi_2\left(2m|r - R|\right) - \chi_2\left(2m|r + R|\right)\right]. \tag{4.17}$$

For a sphere model with radius R, Uehling potential energy is given by two equations. For $r \leqslant R$,

$$V_{\rm Ue}^{\rm (sphere)}(r) = -\frac{\alpha(Z\alpha)}{2\pi m R^3 r} \left[\frac{2}{5} r + \phi\left(2m(R + r)\right) - \phi\left(2m(R - r)\right)\right]. \tag{4.18}$$

For $r > R$,

$$V_{\rm Ue}^{\rm (sphere)}(r) = -\frac{\alpha(Z\alpha)}{2\pi m R^3 r} \times \left[\phi\left(2m(r + R)\right) - \phi\left(2m(r - R)\right) + R\chi_3\left(2m(r - R)\right)\right], \tag{4.19}$$

where

$$\phi(z) = \frac{1}{2} R\chi_3(z) + \frac{1}{4}\chi_4(z), \tag{4.20}$$

and

$$\begin{aligned} 240\chi_3(z) = &\left(33z^2 + z^4\right) K_0(z) + \left(96z - 31z^3 - z^5\right) K_1(z) \\ &- \left(135z - 30z^3 - z^5\right) Ki_1(z) \end{aligned} \tag{4.21}$$

$$\begin{aligned} 1440\chi_4(z) = &\left(225z - 48z^3 - z^5\right) K_0(z) - \left(351z^2 - 46z^4 - z^6\right) K_1(z) \\ &+ \left(225 + 405z^2 - 45z^4 - z^6\right) Ki_1(z). \end{aligned} \tag{4.22}$$

4.3 Wichmann-Kroll correction

Wichmann-Kroll (WK) correction, first introduced by Wichmann and Kroll [19], is a higher order vacuum polarization (VP) correction. In this section, we will first provide a overall theoretical picture of VP, and then discuss the WK calculations together with practical numerical methods to improve the results.

Calculating WK corrections for point-like nuclei are relatively easy. Fainshtein *et al.* [20] expressed WK potential energies for point-like nuclei in terms of piecewise analytic function with respect to nuclear charge number Z. The corresponding WK energy correction can be accurately calculated using this potential energy. However, the point nuclear model is not an appropriate model for precision calculations, since the difference in WK corrections between the point model and other realistic finite-sized nuclear models can be quite large. Therefore, in this section, we focus on calculating the WK corrections with finite-sized nuclear models.

The are two general approaches calculating WK correction with finite-sized nuclei, which correspond to different ways of constructing the bound electron propagator. The first method is constructing the propagator using wavefunctions directly solved from finite basis set (FBS). This method, due to its simplicity, is considered as a robust and numerically efficient but inaccurate method. The second method constructs the propagator using Green function by combining the regular Dirac solutions at the origin $r = 0$ and at infinity $r = \infty$, discussed in Ref. [21, 22]. This method is more accurate but introduce more complexity and is computationally expensive.

In 2023, Salman and Saue [23] demonstrated the feasibility of using FBS method with Gaussian basis to achieve relatively accurate WK calculations. Therefore, In this section, we follow this Gaussian FBS method, and introduce numerical techniques to further improve the accuracy and numerical efficiency of this method.

4.3.1 Theoretical description

To provide an intuitive way to understand VP effect, one can consider that the vacuum as a sea of virtual particles and antiparticles, which are continuously being created and annihilated, arising from the quantum field fluctuations. The virtual particles can be any particle, including the charged particles, e.g. electrons, muons, and hadrons. These charged particles can be polarization by the nuclear charge, such that the virtual positive and negatives charges are spatially separated. This induced VP charge can interact with the atom, causing an energy shift, which is known as the VP effect.

The induced VP charge density in space is denoted as $e\rho^{\mathrm{VP}}(\mathbf{r})$, and $\rho^{\mathrm{VP}}(\mathbf{r})$ can be calculated according to Ref. [19]

$$\rho^{\mathrm{VP}}(\mathbf{r}) = \frac{1}{2}\left[\sum_{E_n>0} \mathrm{Tr}\left(\psi_n^\dagger(\mathbf{r})\psi_n(\mathbf{r})\right) - \sum_{E_n<0} \mathrm{Tr}\left(\psi_n^\dagger(\mathbf{r})\psi_n(\mathbf{r})\right)\right], \tag{4.23}$$

where $\psi_n(\mathbf{r})$ is the wavefunction, including both the radial and angular parts, obtained from solving the Dirac equation with a specific nuclear model, and E_n is its corresponding energy. However, we cannot use this expression to calculate the VP energy correction. The problem is that this expression of $\rho^{\mathrm{VP}}(\mathbf{r})$ does not converge as we sum over more wavefunctions. If one can sum over the infinite amount of wavefunctions, the charge density becomes infinite. In this case, renormalization techniques are required to tame this infinity into a physically meaning observable.

As for WK correction, a higher order VP correction, it does not require renormalization. We can obtain the WK charge density $\rho^{\mathrm{WK}}(\mathbf{r})$ from $\rho^{\mathrm{VP}}(\mathbf{r})$, by subtracting the Uehling term contribution, which is the leading order VP correction. The remaining $\rho^{\mathrm{WK}}(\mathbf{r})$ is convergent with respect to the sum of wavefunctions. Furthermore, according to Eq. (4.1), we know Uehling correction is proportional to charge number Z. Therefore, the Uehling charge density must be linear with respect to Z, and we have

$$\rho_\kappa^{\mathrm{WK}}(r, Z) = \rho_\kappa^{\mathrm{VP}}(r, Z) - \rho_\kappa^{\mathrm{Ue}}(r, Z) \tag{4.24}$$

$$= \rho_\kappa^{\mathrm{VP}}(r, Z) - \lim_{\delta\to 0} \frac{Z}{\delta}\rho_\kappa^{\mathrm{VP}}(r, \delta), \tag{4.25}$$

where $\rho_\kappa(r, Z)$ is the contribution corresponds to wavefunctions with relativistic quantum number $\pm\kappa$ and nuclear charge number Z. The total induced charge density is

$$\rho^{\mathrm{WK}}(r) = \sum_{\kappa=\pm 1}^{\pm\infty} \rho_\kappa^{\mathrm{WK}}(r). \tag{4.26}$$

This expression also applies to $\rho_\kappa^{\mathrm{VP}}(r)$, and $\rho_\kappa^{\mathrm{VP}}(r)$ can be calculated via

$$\rho_\kappa^{\mathrm{VP}}(r) = |\kappa| \sum_n \mathrm{sgn}\left(E_{n,\kappa}\right) \rho_{n,\kappa}^{\mathrm{VP}}(r), \tag{4.27}$$

$$\rho_{n,\kappa}^{\mathrm{VP}}(r) = \frac{1}{4\pi r^2}\left(F_{n,\kappa}^2 + G_{n,\kappa}^2\right), \tag{4.28}$$

where $F_{n,\kappa}/r$ and $G_{n,\kappa}/r$ correspond to the radial wavefunction with quantum number n and κ. The WK charge density $\rho^{\mathrm{WK}}(r)$ can be calculated by combining Eqs. (4.25) to (4.28). One can verify that Eqs. (4.27) and (4.28) are derived from Eq. (4.23), since we have

$$\sum_{m_j=-j}^{j} \mathrm{Tr}\left(\psi_n^\dagger(\kappa m_j;\mathbf{r})\psi_n(\kappa m_j;\mathbf{r})\right) \tag{4.29}$$

$$= \frac{2|\kappa|}{4\pi}\frac{1}{r^2}\left(F_{n,\kappa}^2 + G_{n,\kappa}^2\right), \tag{4.30}$$

where m_j is the magnetic projection of quantum number j. After summing over the angular wavefunctions with different m_j, we obtain the factor $2|\kappa|/(4\pi)$. Combining it with the $1/2$ factor in Eq. (4.23), we arrive at the expressions of Eqs. (4.27) and (4.28).

After knowing $\rho^{\mathrm{WK}}(r)$, WK potential energy can be calculated using

$$V_{\mathrm{WK}}(r) = -4\pi\alpha\left[\frac{1}{r}\int_0^r r'^2\rho^{\mathrm{WK}}\left(r'\right)\,\mathrm{d}r' - \int_r^\infty r'\rho^{\mathrm{WK}}\left(r'\right)\,\mathrm{d}r'\right], \tag{4.31}$$

which is a direction implementation of Eq. (3.13). It should be noted that in natural atomic unit, $4\pi\alpha = e^2$, therefore, the factor of $4\pi\alpha$ can also be replaced by e^2. This WK potential energy can be included in the Dirac equation to calculate the WK energy correction, or one can use the first order perturbation theory, such as

$$E_{\mathrm{WK}} = \langle\psi|\, V_{\mathrm{WK}}\,|\psi\rangle\,. \tag{4.32}$$

Normally, this first order perturbative calculation is sufficiently accurate, since WK is a small correction to the energy levels.

4.3.2 Numerical calculation

We have introduced that WK charge density $\rho^{\mathrm{WK}}(r)$ can be calculated from Eqs. (4.25) to (4.28), and the most important part is getting the radial wavefunctions $F_{n,\kappa}/r$ and $G_{n,\kappa}/r$. The radial wavefunctions can be numerically calculated using variational method with finite basis set discussed in Sec. 2.4.

Gaussian and B-spline basis are two commonly used basis function sets, explained in Sec. 2.4.2 and 2.4.4, respectively. Salman and Saue [23] demonstrated that $\rho^{\mathrm{WK}}(r)$

can be constructed using finite Gaussian basis set. Later, Ivanov *et al.* [24] compared the $\rho^{\mathrm{WK}}(r)$ constructed using Gaussian and B-spline basis, and showed that B-spline basis is not a good choice for this calculation. Therefore, in this section, we are using Gaussian basis to calculate WK charge density $\rho^{\mathrm{WK}}(r)$.

Recall that Gaussian basis functions are defined as

$$\pi_i^{\pm}(r) = \mathcal{N} r^{d_\pm} \exp\bigl(-\zeta_i r^2\bigr), \tag{4.33}$$

where $\mathcal{N}$ is the normalization factor. The parameters $d_\pm$ are

$$d_\pm = \left|\kappa \pm \frac{1}{2}\right| + \frac{1}{2}, \tag{4.34}$$

and ζ_i coefficients must follow

$$\zeta_i = \zeta_1 \left(\zeta_N/\zeta_1\right)^{\frac{i-1}{N-1}}, \tag{4.35}$$

where N is the number of functions in the basis set. For WK calculations, the coefficients ζ_1 and ζ_N are slightly different from those used in Sec. 2.4.2

$$\begin{gathered} \zeta_1 = 1/\left(2\,r_1^2\right),\ \zeta_N = 1/\left(2\,r_N^2\right), \\ r_1 = r_{\mathrm{rms}}/20,\ r_N = r_{\mathrm{B}}/7, \end{gathered} \tag{4.36}$$

where r_{rms} is the rms nuclear charge radius and r_{B} is the Bohr radius. This choice of ζ_1 and ζ_N is empirically determined, showing a good performance at both small and large nuclear charge number Z.

As discussed in Sec. 2.4.3, theoretically speaking, the wavefunctions should always satisfy charge conjugation symmetry, denoted as $\mathcal{C}$ symmetry. However, numerically calculated wavefunctions might slightly violate $\mathcal{C}$ symmetry, and the dual kinetic balance (DKB) approach can be used to ensure $\mathcal{C}$ symmetry. Alternatively, one can also enforce $\mathcal{C}$ symmetry by using

$$\rho_{\kappa,\mathcal{C}}(r, Z) = \frac{1}{2}\left[\rho_\kappa(r, Z) - \rho_\kappa(r, -Z)\right], \tag{4.37}$$

where $\rho_{\kappa,\mathcal{C}}(r, Z)$ is the charge density satisfying $\mathcal{C}$ symmetry.

In Sec. 2.4.2, we discussed how to construct and diagonalize the radial Hamiltonian under Gaussian basis to obtain energies and wavefunctions. WK charge density is calculated using the result and presented in Fig. 4.3. The figure shows $\rho^{\mathrm{WK}}(r)$ of hydrogen-like Pb together with different $|\kappa|$ contributions calculated using $N = 150$ Gaussian basis functions. One can see that at small distance, the charge density is negative, whereas at large distance, it is positive. This is because the total charge integrated over all space should be zero, which means $\rho^{\mathrm{WK}}(r)$ must satisfy

$$\int_0^\infty \rho_\kappa(r) r^2 \,\mathrm{d}r = 0, \tag{4.38}$$

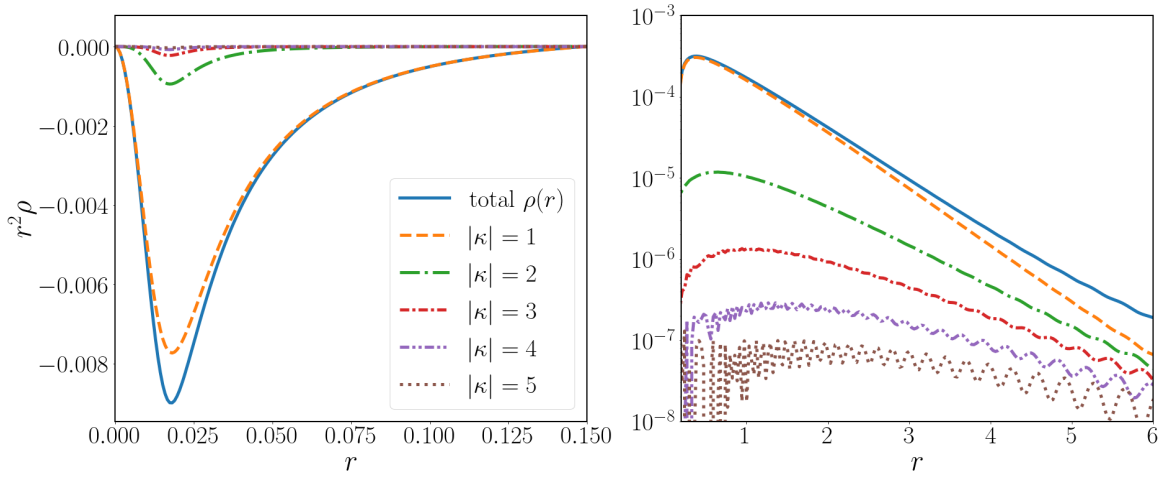

Figure 4.3: **WK charge density $\rho^{\mathrm{WK}}(r)$ of hydrogen-like Pb ($Z = 82$).** The results show different $|\kappa|$ contributions at small (left) and large (right) distance, in natural unit ($c = m_e = \hbar = \varepsilon_0 = 1$), where m_e is the electron mass. The results are calculated using FBS method with $N = 160$ Gaussian basis functions and the sphere nuclear model with $r_{\mathrm{rms}} = 5.273$ fm.

for any κ. This can be used as a validity check of the results.

As shown in Fig. 4.3, $\rho^{\mathrm{WK}}(r)$ has incorrect oscillatory behavior at large distance, and it is particularly obvious for large $|\kappa|$. This oscillation can be mitigated by increasing N but cannot be completely eliminated. However, we introduce a dual basis construction (DBC) method to address it. Since this oscillation is basis dependent, i.e. changing the positions and densities of basis functions will alter the oscillation, one can construct a second basis with "opposite oscillation phase" to cancel it. To do this, we choose $2N$ numbers of $\{\zeta_i\}$ coefficients and separate them into two sets, even labeled $\{\zeta_{2i}\}$ and odd labeled $\{\zeta_{2i+1}\}$. This creates two sets of basis, and each has N number of functions. We calculate $\rho_\kappa(r)$ twice using two basis and take the average result, which exhibits a smooth plot, as shown in Fig. 4.4.

Regarding the accuracy, the result should converge to the correct value when the basis is complete, and ideally, the basis becomes complete when

$$\zeta_1 \to \infty \tag{4.39}$$

$$\zeta_N \to 0 \tag{4.40}$$

$$\left(\frac{\zeta_1}{\zeta_N}\right)^{1/(N-1)} \to 1^+ \tag{4.41}$$

$$N \to \infty. \tag{4.42}$$

The four conditions are investigated respectively. Since ζ_i approximately determines the location of i-th basis function, conditions (4.39) and (4.40) indicate that the

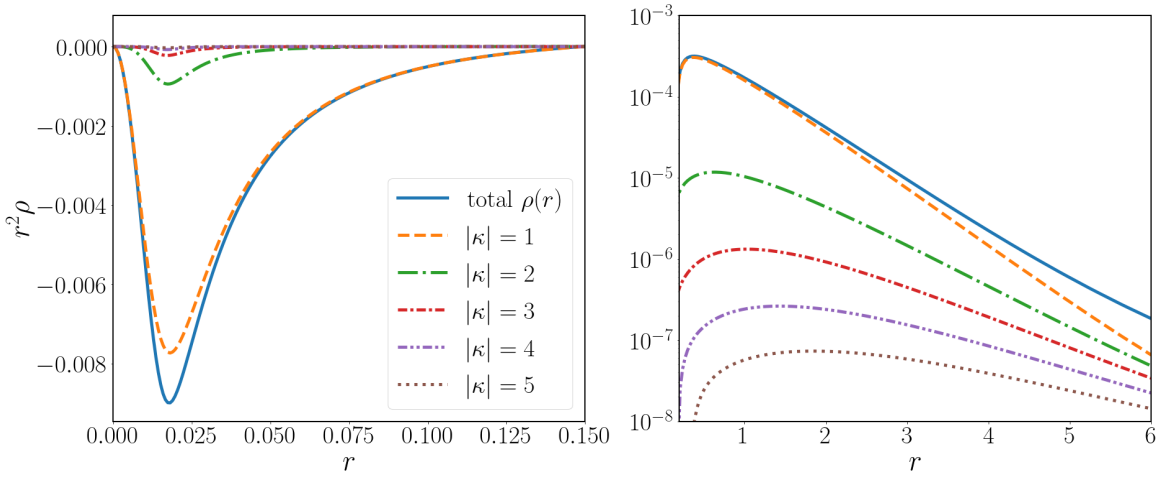

Figure 4.4: **WK charge density $\rho^{\mathrm{WK}}(r)$ of hydrogen-like Pb ($Z = 82$) with DBC method.** The results are calculated using $N = 160$ Gaussian basis functions and DBC method.

location of the first basis function should be sufficiently close to the origin, whereas the N-th basis function should be sufficiently far from it. We choose ζ_1 such that the maximum value of the first basis function is located inside the nucleus. Similarly, the value of ζ_N is determined such that the maximum value of the N-th basis function is located at r where $\rho^{\mathrm{WK}}(r) \to 0$. Therefore, in Eq. (4.36), ζ_1 and ζ_N are determined according to r_{rms} and r_{B}, respectively. Conditions (4.41) and (4.42) make sure that the basis sufficiently span the space. Condition (4.41) focuses on the density of the basis functions, whereas condition (4.42) is only about the number. With the choice of ζ_1 and ζ_N defined by Eq. (4.36), we have

$$\left(\frac{\zeta_1}{\zeta_N}\right)^{1/(N-1)} \approx 1.14, \text{ with } N = 160. \tag{4.43}$$

These are the parameters used in the WK calculation after numerical investigating a wide range of parameters. The results of the calculation are presented in Table 4.1 with literature comparisons, and the numerical convergence is discussed.

With the Gaussian basis parameters introduced above, in principle, one can continuously improve the numerical accuracy of the results by increasing N. However, this leads to additional numerical problems. The first numerical problem is that double precision is no longer sufficient to construct a linearly independent Gaussian basis at large N. This is also discussed in Sec. 2.4.2. Double precision refers to the floating-point number format which is occupying 64 bits of computer memory, and in terms of decimal numbers, it normally corresponds to 15 to 17 significant digits. When N is large enough, e.g. $N \gtrapprox 50$ in our case, the Gaussian basis constructed using double precision becomes linearly dependent, and therefore, the Hamiltonian is

	Z	r_{rms} (fm)	$1s_{1/2}$	$2s_{1/2}$	$2p_{1/2}$	$2p_{3/2}$	
Kr	36	4.230	0.01550	0.00200	0.00006	0.00002	
			0.01550	0.00200	0.00006	0.00002	*a*
Xe	54	4.826	0.1695	0.0230	0.0016	0.0004	
			0.1695	0.0230	0.0016	0.0004	*a*
Yb	70	5.273	0.8283(3)	0.1198	0.0153	0.0028	
			0.8283	0.1198	0.0153	0.0028	*a*
Pb	82	5.505	2.2901(8)	0.3534(1)	0.0661	0.0094	
			2.2900	0.3534	0.0660	0.0094	*a*
			2.2898	0.3534	0.0660	0.0094	*b*
U	92	5.860	4.9859(11)	0.8212(2)	0.2058(1)	0.0226	
			4.9863	0.8214	0.2057	0.0226	*a*
			4.9860	0.8213	0.2056	0.0225	*b*

a Adopted from Ref. [25].

b Adopted from Ref. [26].

Table 4.1: **WK energy corrections (eV) for various electronic hydrogen-like ions.** The results are calculated from spherical nuclear models, using $N = 160$ and $|\kappa|_{\max} = 5$. Numbers in parenthesis indicate the likelihood of convergence, calculated from the difference between results using $N = 150$ and 160. Numbers of this work without parenthesis refer to no difference in the reported precision.

not diagonalizable. To tackle this problem, We use mpmath [10], a Python library for arbitrary-precision floating-point arithmetic, and increased the numerical precision to 50 decimal places. This allows us to perform the calculation with $N = 160$ basis functions and relativistic quantum number up to $|\kappa|_{\max} = 5$.

The second numerical problem is that while increasing N, it is still not feasible to have sufficiently dense Gaussian basis function at large distance r. Therefore, WK charge density $\rho^{\mathrm{WK}}(r)$ is slightly inaccurate at large r. This problem cannot be efficiently addressed by increasing N. We will tackle it with the help of the analytic WK potential of point-like nuclei. At sufficiently large distance r, the finite-sized nucleus can be considered as a point-like nucleus, and its corresponding $V_{\mathrm{WK}}(r)$ can be approximated by a point nuclear model.

The WK potential energy for point-like nuclei can be expressed as piecewise analytic functions, as shown in Ref. [20]. By using this method, we present $V_{\mathrm{WK}}(r)$ for both point and sphere nuclear models in Fig 4.5. While the two models offer distinct $V_{\mathrm{WK}}(r)$ at small r, their values converge at large r. At sufficiently large r, our calcu-

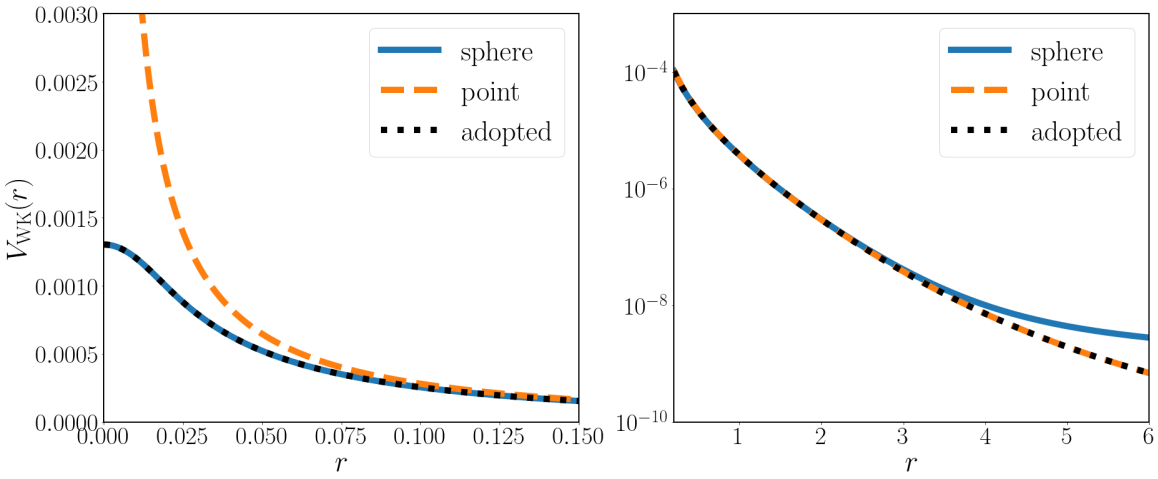

Figure 4.5: **WK potential energy $V_{\mathrm{WK}}(r)$ of hydrogen-like Pb.** The two plots show $V_{\mathrm{WK}}(r)$ at small (left) and large (right) distance. The results are calculated from point and sphere nuclear models. The black dotted line is the $V_{\mathrm{WK}}(r)$ adopted in our calculation.

lated $V_{\mathrm{WK}}(r)$ of the sphere model experiences numerical noise, and its value deviates from the expected exponential decay. In this region, we adopt the analytic results from the point model instead.

4.4 Källén-Sabry correction

Introduced by Källén and Sabry [27], Källén-Sabry correction was initially named as the fourth order VP correction. It is a two-loop VP effect, which is different from the one-loop Uehling and WK corrections.

4.4.1 Arbitrary nuclear model

Källén-Sabry potential energy for arbitrary spherically symmetric nuclear charge distribution, $\rho(r)$, is given by

$$V_{\mathrm{KS}}(r) = -\frac{\alpha^2(Z\alpha)}{\pi m r}\int_0^\infty dr'\, r'\rho(r')\left[L_0\left(2m|r-r'|\right) - L_0\left(2m|r+r'|\right)\right], \tag{4.44}$$

where Z is the nuclear charge number, and m is the mass of the particle. The function $L_0(x)$ is defined as

$$L_0(x) = -\int^x dt\, L_1(t), \tag{4.45}$$

where

$$L_1(x) = \int_1^\infty dt \exp(-xt) \Bigg[\left(\frac{2}{3t^5} - \frac{8}{3t} \right) f(t) + \left(\frac{2}{3t^4} + \frac{4}{3t^2} \right) \sqrt{t^2-1} \ln\left(8t^3 - 8t\right) + \left(\frac{2}{9t^6} + \frac{7}{108t^4} + \frac{13}{54t^2} \right) \sqrt{t^2-1} + \left(\frac{2}{9t^7} + \frac{5}{4t^5} + \frac{2}{3t^3} - \frac{44}{9t} \right) \ln\left(\sqrt{t^2-1} + t \right) \Bigg], \tag{4.46}$$

and

$$f(x) = \int_x^\infty dt \left[\frac{(3t^2-1)\ln\left(\sqrt{t^2-1}+t\right)}{t(t^2-1)} - \frac{\ln(8t^3-8t)}{\sqrt{t^2-1}} \right]. \tag{4.47}$$

The calculation includes many layers of integration, which is extremely difficult to calculate. It is necessary to apply numerical approximate method to this calculation.

Blomqvist [28] originally introduced this method to calculate $L_1(x)$, and Fullerton *et al.* [29] provided Chebyshev polynomial approximations for both $L_1(x)$ and $L_0(x)$. Later, Indelicato [30] provided a more accurate version of it, which is summarized as follows.

For $x \leqslant 3$,

$$L_0(x) = x h_2(x) \ln^2(x) + x h_1(x) \ln(x) + h_0(x), \tag{4.48}$$

where

$$\begin{aligned} h_0(x) = {} & 2.005566300 - 2.39716878893\, x \\ & + 1.04324860906\, x^2 - 0.36332915853\, x^3 \\ & + 0.063004651772\, x^4 - 0.038046259798\, x^5 \\ & + 0.0008743378646\, x^6 - 0.00036443366062\, x^7 \\ & + 0.000015791745043\, x^8 - 0.00001608988362060\, x^9, \end{aligned} \tag{4.49}$$

$$\begin{aligned} h_1(x) = {} & 0.7511983817345282548 + 0.13888763396658555408\, x^2 \\ & + 0.020975409736870016795\, x^4 + 0.00017561631242035479319\, x^6 \\ & + 9.057708511987165794 \times 10^{-6}\, x^8, \end{aligned} \tag{4.50}$$

and

$$\begin{aligned} h_2(x) = {} & -0.44444444460943167625 - 0.0034850996339125316319\, x^4 \\ & - 1.4173521392055667219 \times 10^{-6}\, x^8. \end{aligned} \tag{4.51}$$

For $x > 3$,

$$\begin{aligned} L_0(x) = {} & 41.1352787432251923 \\ & - 5.1094977559522696 \Big[8.05074798111 \operatorname{erf}\left(\sqrt{x}\right) \\ & - 1.028091975364 \operatorname{Ei}(-x) \\ & + \frac{e^{-x}}{x^{5/2}} \Big(- 2.02809197536\, x^{3/2} + 4.54214815071\, x^2 \\ & - 0.494718704003\, x + 0.98439728916\, \sqrt{x} \\ & - 0.344009752879 \Big) \Big], \end{aligned} \tag{4.52}$$

where $\operatorname{erf}(x)$ is the error function, and $\operatorname{Ei}(x)$ is the exponential integral.

Similarly to other corrections, KS correction can be calculated by including its potential energy into the Dirac equation. Alternatively, it can also be calculated perturbatively using the wavefunction from the Dirac equation.

4.4.2 Point, shell, and sphere models

Källén-Sabry potential energy for a point-like nucleus is given by

$$V_{\mathrm{KS}}^{(\mathrm{point})}(r) = -\frac{\alpha^2(Z\alpha)}{\pi m r} L_1(2mr), \tag{4.53}$$

where Z is the nuclear charge number, and m is mass of the particle. The function $L_1(x)$ is defined by Eq. (4.46), and according to [30], it can be calculated as follows.

For $x \leqslant 3$,

$$L_1(x) = g_2(x) \ln^2(x) + g_1(x) \ln(x) + g_0(x), \tag{4.54}$$

where

$$\begin{aligned} g_0(x) = {} & 1.6459704071917522632 - 2.0864972181198001792\, x \\ & + 0.95109984162919008905\, x^2 - 0.25201860708873574898\, x^3 \\ & + 0.16925588925254111005\, x^4 - 0.005246027187885263513 2\, x^5 \\ & + 0.0023754193119115541914\, x^6 - 0.0001263339603419473189 1\, x^7 \\ & + 0.0001357512440733955030 7\, x^8, \end{aligned} \tag{4.55}$$

$$\begin{aligned} g_1(x) = {} & 0.13769050748433509769 - 0.41666290189975666225\, x^2 \\ & - 0.097906849416525020713\, x^4 - 0.0012293141869424835524\, x^6 \\ & - 0.0000786846723294733586 99\, x^8, \end{aligned} \tag{4.56}$$

and

$$g_2(x) = 0.44444444460943167625 + 0.017425498169562658160\,x^4 - 0.00001275616925285010049 7\,x^8. \tag{4.57}$$

For $x > 3$,

$$L_1(x) = \frac{e^{-x}}{x^{7/2}}\Big(4.3942926509010 - 10.059551479890\,x^{1/2} + 5.5493632222582\,x + 5.3327556570422\,x^{3/2} - 9.0762837836987\,x^2 + 5.1094977559523\,x^{5/2}\Big). \tag{4.58}$$

For a shell nuclear model with radius R, Källén-Sabry potential energy is given by

$$V_{\mathrm{KS}}^{(\mathrm{shell})}(r) = -\frac{\alpha^2(Z\alpha)}{4\pi^2 mRr}\left[L_0\left(2m|r-R|\right) - L_0\left(2m|r+R|\right)\right], \tag{4.59}$$

where the function $L_0(x)$ can be evaluated using Eqs. (4.48) to (4.52).

For sphere nuclear models, Källén-Sabry potential energy can be expressed similarly to Eqs. (4.18) and (4.19), which are equations for Uehling potential energy of sphere models. However, since the numerical method in Sec. 4.4.1 is already very efficient, one can use Eq. (4.44) for arbitrary models and apply it to sphere models.

4.5 Muonic and hadronic vacuum polarization

As shown in earlier sections, the equations for Uehling and KS potential energies explicitly depend on mass of the particle m. Although less apparent, WK potential energy also depends on m, since the WK charge density is derived from wavefunctions depending on m. Here, m denotes the mass of virtual particle being polarized in the vacuum. In principle, it can be any charged particle. However, unless otherwise specified, it conventionally refers to electron. This is because electronic VP correction yields the dominant contribution among VP corrections caused by other virtual particles.

Muonic VP correction is typically two orders of magnitude smaller than electronic VP correction, since muon has roughly 207 times larger mass. It can be calculated by using the same equations or numerical methods by adopting the muon mass. However, hadronic VP corrections cannot be calculated using the same way by simply changing the value of mass. Hadrons can interact via the strong force, making the calculation much more challenging. Consequently, semi-empirical approach are required in the calculation.

Hadronic Uehling calculation is investigated by Breidenbach *et al.* [31]. For a sphere nuclear model with radius R, hadronic Uehling potential energy can be expressed, in natural unit, as the following. For $r \leqslant R$,

$$\begin{aligned} V_{\text{had}}^{(\text{sphere})}(r) = &- \frac{3Z\alpha B_1\sqrt{C_1}}{rR^3}\Bigg\{\sqrt{C_1}\,r + \sqrt{C_1}RE_3\left(\frac{r+R}{\sqrt{C_1}}\right) + C_1E_4\left(\frac{r+R}{\sqrt{C_1}}\right) \\ &- \frac{1}{6}\exp\left(\frac{r-R}{\sqrt{C_1}}\right)\left[2C_1 + \sqrt{C_1}\,(r+2R) + (r-R)\,(r+2R)\right] \\ &- \frac{(r-R)^2(r+2R)}{6\sqrt{C_1}}\,E_1\left(\frac{R-r}{\sqrt{C_1}}\right)\Bigg\}, \end{aligned} \tag{4.60}$$

where Z is the nuclear charge number, B_1 and C_1 are two parameters given by

$$B_1 = 0.0023092, \quad C_1 = \left(3.9925370\ \text{GeV}^{-2}\right)\left(mc^2\right)^2, \tag{4.61}$$

and here, m corresponds to the unit system. It is the electron mass in electronic natural unit and muon mass in muonic natural unit. Additionally, $E_n(x)$ denotes the exponential integral

$$E_n(x) = \int_1^\infty \frac{e^{-xt}}{t^n}\,\mathrm{d}t. \tag{4.62}$$

For $r > R$,

$$V_{\text{had}}^{(\text{sphere})}(r) = -\frac{3Z\alpha B_1\sqrt{C_1}}{rR^3}\left[\sqrt{C_1}\,RD_3^+(r,R) - C_1D_4^-(r,R)\right], \tag{4.63}$$

where $D_n^\pm(r,x)$ are functions defined as

$$D_n^\pm(r,x) = E_n\left(\frac{|r-x|}{\sqrt{C_1}}\right) \pm E_n\left(\frac{r+x}{\sqrt{C_1}}\right). \tag{4.64}$$

Finally, the hadronic Uehling correction for energy can be obtained by including this potential energy into the Dirac equation. Alternatively, it can also be calculated perturbatively using the wavefunction from the Dirac equation.

4.6 Other corrections

For muonic atoms, vacuum polarization is the dominant correction among all other QED effects. Whereas, for normal electronic atoms, vacuum polarization and self-energy corrections have comparable magnitudes, surpassing other corrections. The complexity of rigorous self-energy calculation is comparable to all vacuum polarization contribution combined, and therefore lies beyond the scope of this thesis. The method is introduced in Ref. [21, 32–34].

Nuclear polarization and relativistic recoil corrections, although relatively smaller than vacuum polarization, are important to have a correct description of muonic

atom transition energies. The method for nuclear polarization calculation is given by Ref. [35], whereas relativistic recoil is detailed in Ref. [36].

Screening effect is a small correction specific to muonic atoms, arising from the interaction between the bound muon and the existing electrons. While the muon stay very close to the nucleus, the electronic wavefunctions are much further away from the muon. In addition to the nuclear potential, the muon experiences an electric screening potential provided by the outer electrons. This screening potential can be calculated using the same method applied to the nuclear potential, but instead of adopting the electron charge distribution derived from the many-body electronic wavefunction. In practice, most outer electrons contribute an approximately constant energy shift to all of the low-lying muonic states. The net effect on a transition energy is therefore determined by the difference in screening corrections between the two states, which becomes negligible. As a result, for screening potential calculation, it is sufficient to consider only the charge density of the two $1s_{1/s}$ electrons, which significantly simplifies the problem.

Chapter 5

Nuclear charge radius determination

The root-mean-square (rms) nuclear charge radius is an important benchmark for various fields of physics and chemistry. The nuclear charge distribution directly maps the proton distribution within the nucleus, offering a sensitive test for the models of nuclear structure. It is a crucial parameter for nuclear physics to investigate nuclear models and shapes. Since the charge radius directly affects the energy levels of atoms, it is also the prerequisite parameter for the precision tests of quantum electrodynamics (QED) and the determination of bound state g-factors. Furthermore, its importance extends to astrophysics, e.g. it serves as a fundamental input parameter for the theory of the rapid neutron-capture process (r-process). Therefore, it is important to have accurate and precise determinations of nuclear charge radii, and this heavily relies on the precision calculations of atomic binding energies and the QED corrections discussed in the previous chapters.

It is extremely challenging to calculate nuclear charge distribution from first principle, particularly for heavy nuclei. Moreover, this distribution cannot be measured directly. Therefore, determining the nuclear charge radius always requires a combined effort from both theoretical and experimental efforts.

This chapter begins with an introductory overview of different methods evaluating nuclear charge radius. Next, we focus on elaborating the muonic atom spectroscopy method. Then, we introduce the fine-structure anomaly in the study of muonic ^{208}Pb nuclear radius, which manifests as a discrepancy between theoretical calculation and experimental measurement, exceeding the predicted uncertainty. A dedicated section for fitting and uncertainty analysis therefore follows. Finally, we present our evaluation of the ^{208}Pb rms nuclear charge radius using state-of-the-art theoretical calculations combined with a systematic uncertainty analysis. Our result shows a

significant reduced fine-structure anomaly, and the goodness of fit is improved by a factor of twenty. This result is discussed and compared with other values from the literature.

5.1 Overview

There are different ways to determine rms nuclear charge radius, and electron scattering is one of the common methods. In this method, a beam of high-energy electrons is fired at the target nucleus and measures the scattering probability as a function of angle. This is equivalent of measuring the differential cross-section as a function of angle. It is assumed that the electrons only interact with the nucleus via electromagnetic force. In this case, the measured differential cross-section as a function of angle can be converted to the form factor as a function of momentum transfer, namely the momentum that the electron gives to the nucleus. Finally, the form factor in momentum space can be Fourier transformed into nuclear charge distribution in coordinate space.

This electron scattering method not only determines the rms nuclear charge radius, but also provides the complete the nuclear charge distribution along the radial direction. Therefore, in principle, this is a model-independent method. However, in practice, the measured data does not present as a smooth analytic function. One needs to fit the data with respect to a specific nuclear model, and different nuclear model can result in slightly different goodness of fit and nuclear radius. Therefore, the outcome of this method can be model-dependent.

The second method is muonic atom spectroscopy. Owing to the muon's significantly heavier mass, its Bohr orbit is much smaller than that of an electron, bringing it much closer to the nucleus. Consequently, the transition energies of muonic atoms are highly sensitive to the spatial distribution of the nuclear charge, making them ideal probes for nuclear radius determination. By calculating the binding energies and all relevant QED corrections with a given nuclear model, one can derive the theoretical transition energies as functions of nuclear charge radius. Combining the theoretical calculation with the experimentally measured transitions allows for a precise determination of the rms nuclear charge radius.

Clearly, this muonic atom spectroscopy is a model-dependent method. However, for a given set of measured transition energies, one can fit it with respect to various nuclear models, yielding different goodness of fit correspondingly. A relatively better fit indicates the corresponding nuclear model is more realistic compared to others, and the model dependence of the result can be indirectly studied via this way.

Comparing the two methods, they offer complementary approaches with distinct advantages. The electron scattering method directly probes the nuclear properties, providing more insight to the spatial distribution of nuclear charge. The muonic atom spectroscopy method determines the rms nuclear charge radius with relatively higher precision, but only allows indirect investigation of nuclear model dependence of the result. In the following sections, rms nuclear charge radius of ^{208}Pb will be determined from muonic atom spectroscopy, and the results will be compared with other literature values in detail.

It should be noted that measuring the isotope shift is another powerful method for determining the relative nuclear charge radius. If the rms nuclear charge radius of a specific reference isotope is known, this method enable the determination of relative radius changes for other isotopes. The isotope shift arises from two primary contributions, the mass shift, due to differences in nuclear mass between isotopes, and the field shift, which originates from differences in nuclear charge radius. By isolating the field shift effect from the mass shift, isotope shift measurement allows for the extraction of nuclear charge radii for short-lived radioactive isotopes that are inaccessible to other methods. However, in this thesis, we will not elaborate further on this method, as its application requires a known radius determined from another approach, placing it outside the scope of our study.

5.2 Muonic atom spectroscopy

Similar to the electron, muon is a charged lepton, but has a mass approximately 207 times larger than the electron. It is an unstable subatomic particle with a mean lifetime of roughly 2.2 μs. This is a relatively long lifetime by the subatomic standard. A muon can replace one or more electrons in a normal atom, turning it into a muonic atom. Due to muon's large mass, its wavefunction is localized much closer to the nucleus compared to the other electrons. This effect is evident from the Bohr radius r_0 of hydrogen-like atoms, given by

$$r_0 = \frac{\hbar}{Zm\alpha}, \tag{5.1}$$

in natural unit, where Z is the nuclear charge number, m is the mass of the particle, and α is the fine-structure constant. The Bohr radius approximates the most probable distance for the $1s_{1/2}$ wavefunction from a point-like nucleus, and its value is inversely proportional to mass of the particle.

As a more direct way to view it, the probability distribution of muonic and electronic wavefunctions for lead (Pb) are compared and presented in Fig. 5.1. In the

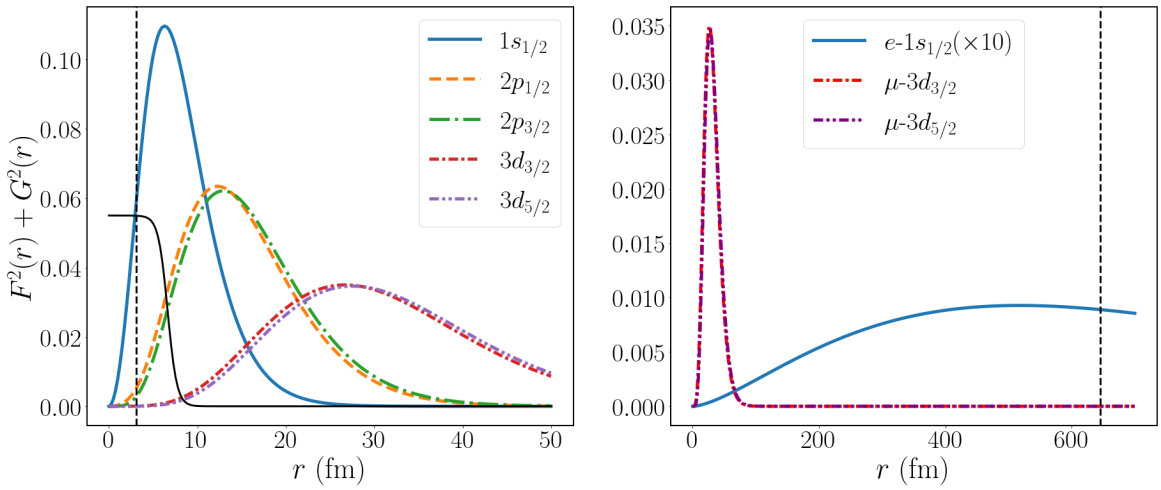

Figure 5.1: **Muonic and electronic wavefunctions of Pb.** The muonic wavefunctions (left) are compared with an amplified electronic wavefunction (right). The results are calculated from a 2pF nuclear model with $r_{\text{rms}} = 5.5$ fm, and the nuclear charge distribution is plotted as a solid black line. The two vertical dashed black lines indicate the Bohr radii of hydrogen-like muonic Pb (left) and electronic Pb (right).

figure, the wavefunctions are plotted as a function of distance in unit of fm, with the Bohr radii of the corresponding muonic and electronic atoms also indicated. The results are calculated from a finite-sized nucleus with a rms charge radius of 5.5 fm. The Bohr radii in the figure do not align with the maximum values of the $1s_{1/2}$ wavefunctions, and this corresponds to the difference between point-like and finite-sized nucleus. The figure shows that the muonic wavefunctions are very close to the nucleus and partially overlapping with the nuclear charge distribution. This makes muonic atoms an excellent probe for measuring nuclear properties. Furthermore, since the muonic wavefunction is spatially separated from the electrons, the muon-electron interactions are very small. Additionally, it is unlikely for an atom to capture more than one muon due to muon's short lifetime. This renders the muonic atom effectively hydrogen-like, enabling highly precise theoretical calculations of its energy levels.

To measure the transition energies of muonic atoms, a beam of negative muons is directed at the target material, e.g. a solid foil of the element being measured. An atom can capture a muon and become a short-lived muonic atom. The captured muon starts in a high energy bound state and rapidly cascades down through the atomic orbitals towards the $1s_{1/2}$ ground state. During this cascade, the muon can either eject the atom's original electrons via Auger process or emit characteristic X-ray to reach lower levels. As the muon reaches sufficiently low orbitals, the X-ray emissions become the dominant decay mode. By measuring these X-ray with high precision, the transition energies of the muonic atom can be determined.

Transition	Bergem 1988	Hoehn 1984	Kessler 1975	Anderson 1969
$2p_{3/2} - 1s_{1/2}$	5962.854(90)		5962.770(420)	5963.770(450)
$2p_{1/2} - 1s_{1/2}$	5778.058(100)		5777.910(400)	5778.930(500)
$3d_{5/2} - 2p_{1/2}$	2642.332(30)	2642.274(23)	2642.110(60)	2641.480(300)
$3d_{5/2} - 2p_{3/2}$	2500.590(30)	2500.564(28)	2500.330(60)	2500.070(450)
$3d_{3/2} - 2p_{3/2}$	2457.569(70)		2457.200(200)	2456.640(470)
$3p_{3/2} - 2s_{1/2}$	1507.754(50)		1507.480(260)	
$3p_{1/2} - 2s_{1/2}$	1460.558(32)			
$2s_{1/2} - 1s_{1/2}$	1215.330(30)		1215.430(260)	
$2s_{1/2} - 2p_{3/2}$	1030.543(27)		1030.440(170)	

Retrieved from Ref. [7, 9, 37, 38].

Table 5.1: **Literature values for transition energies (keV) of muonic ^{208}Pb.**

In Table 5.1, a list of transition energy measurements [7, 9, 37, 38] of muonic ^{208}Pb are presented. The transition energies of muonic atoms are on the order of MeV. The tabulated data show good consistency across different experimental measurements within their reported uncertainties, with later experiments generally having better precision. These experimental data can be combined with theoretical calculations in a fitting procedure to determine the nuclear charge radius. However, for ^{208}Pb, such a fit yields poor agreement for arbitrary nuclear radius. This discrepancy is known as the fine-structure anomaly of muonic ^{208}Pb, which will be discussed in the next section.

5.3 The ^{208}Pb fine-structure anomaly

The isotope ^{208}Pb is one of the four stable isotopes of lead. It is a very special isotope, since it is the heaviest stable nuclei known, and it is also the heaviest doubly magic nuclide. A doubly magic nuclide has proton and neutron numbers both equal to one of the magic numbers: 2, 8, 20, 28, 50, 82, and 126. These numbers represent closed nuclear shells, similar to filled electron shells. With 82 protons and 126 neutrons, ^{208}Pb satisfies this condition. Normally, doubly magic nuclides have very spherical nuclear shapes, excluding themselves from the sophisticated nuclear deformation effects. For instance, ^{208}Pb has a very small nuclear deformation parameter, $\beta \approx 0.05$, which is defined in Sec. 3.4. In addition, muonic ^{208}Pb has relatively small coupling between its muonic and nuclear states. In principle, this should enable precise determination of the nuclear charge radius of ^{208}Pb. However, the fit between experimental and theoretical

	Bergem *et al.*[a]			This work	
Transition	Experiment	Theory	$\|\Delta E\|$	Theory	$\|\Delta E\|$
$2p_{3/2} - 1s_{1/2}$	5962.854(90)	5962.943	0.089	5962.784	0.070
$2p_{1/2} - 1s_{1/2}$	5778.058(100)	5777.831	0.227	5777.779	0.279
$3d_{5/2} - 2p_{1/2}$	2642.332(30)	2642.478	0.146	2642.363	0.031
$3d_{5/2} - 2p_{3/2}$	2500.590(30)	2500.385	0.205	2500.371	0.219
$3d_{3/2} - 2p_{3/2}$	2457.569(70)	2457.366	0.203	2457.358	0.211
$3p_{3/2} - 2s_{1/2}$	1507.754(50)	1508.037	0.283	1508.074	0.320
$3p_{1/2} - 2s_{1/2}$	1460.558(32)	1460.506	0.052	1460.593	0.035
$2s_{1/2} - 1s_{1/2}$	1215.330(30)	1215.543	0.213	1215.394	0.064
$2s_{1/2} - 2p_{3/2}$	1030.543(27)	1030.431	0.112	1030.389	0.154

[a] Retrieved from Ref. [9].

Table 5.2: **Experimental and theoretical transition energies (keV) of muonic ^{208}Pb.** The theoretical values are caculated from the best-fit nuclear parameters, and $|\Delta E|$ is the magnitude of their difference with respect to the experimental values.

results show poor agreement, and this is known as the fine-structure anomaly of ^{208}Pb.

This fine-structure anomaly was discovered and studied by Bergem *et al.* [9] in 1988. The study not only experimentally measured the muonic ^{208}Pb transition energies, but also theoretically calculated the energies as functions of nuclear parameters. By performing a χ^2 fit between the experimental and theoretical results, the rms charge radius was determined. The results of transition energies are presented in Table 5.2, while the best-fit nuclear parameters and the resulting rms radius are given in Table 5.3. Using the two-parameter Fermi (2pF) nuclear model, Bergem *et al.* fitted the results with respect to Fermi a and c parameters, as defined in Sec. 3.3. The goodness of the fit is quantified by χ^2 per degree of freedom (DoF). A smaller χ^2/DoF corresponds to a better fit, where $\chi^2/\text{DoF} \leqslant 1$ is considered the fit in agreement within uncertainties. However, as shown in Table 5.3, Bergem *et al.* reported a $\chi^2/\text{DoF} = 187$, signaling a significant discrepancy.

This anomalous result was attributed to the least understood and the most difficult correction: nuclear polarization (NP). This effect originates from the interaction between the nucleons and the bound muon (or electron). A rigorous treatment would require complete knowledge of both the muonic and the many-body nuclear state. However, *ab initio* calculation of nuclear states for heavy atoms is nearly impossible. As a result, calculations of nuclear polarization must rely on nuclear parameters obtained through approximated methods, which significantly limits the accuracy.

	c (rm)	a (rm)	$r_{\rm rms}$ (rm)	χ^2/DoF
Bergem *et al.*[a]	6.6447(5)	0.5249(3)	5.5040(11)	187
This work[b]	6.6409(25)	0.5283(18)	5.5062(5)	9.5

[a] Retrieved from Ref. [9].

[b] Published as Ref. [2].

Table 5.3: **Best-fit nuclear parameters for ^{208}Pb.**

After several decades, much more robust methods for NP calculation have been developed, e.g. Ref. [35]. Meanwhile, the methods for other corrections also have modest improvements. We combined the latest numerical techniques and reevaluated the nuclear charge radius of ^{208}Pb using the similar fitting procedure. The results, shown in Tables 5.2 and 5.3, are presented in comparison with Bergem's results.

		Vacuum polarization								
State	FNS	Ue	WK	KS	μUe	HUe	SE	NP	RRecoil	Scrn
$1s_{1/2}$	10525.905	67.084	-0.504	0.552	0.238	0.159	-3.345(50)	5.712(603)	-2.555(66)	5.555
$2s_{1/2}$	3581.659	19.336	-0.250	0.149	0.041	0.027	-0.653(6)	1.063(156)	-1.317(27)	5.536
$2p_{1/2}$	4783.784	32.290	-0.356	0.251	0.044	0.030	-0.440(20)	1.923(263)	-2.114(4)	5.548
$2p_{3/2}$	4601.766	29.761	-0.344	0.229	0.033	0.023	-0.745(10)	1.864(256)	-2.172(2)	5.547
$3p_{1/2}$	2129.324	10.759	-0.167	0.081	0.014	0.009	-0.180(15)	0.584(99)	-1.003(3)	5.512
$3p_{3/2}$	2082.436	10.230	-0.163	0.077	0.011	0.008	-0.245(10)	0.619(96)	-1.025(0)	5.510
$3d_{3/2}$	2163.565	10.502	-0.192	0.076	0.001	0.001	0.020(2)	0.238(56)	-1.162(1)	5.525
$3d_{5/2}$	2121.477	9.848	-0.185	0.071	0.001	0.000	-0.070(5)	0.037(37)	-1.143(0)	5.523

Published as Ref. [2].

Table 5.4: **Corrections to the binding energies (keV) of muonic ^{208}Pb.** The results are calculated perturbatively with FNS wavefunctions. A positive correction refers to an increase in binding energy.

All relevant corrections to the binding energies of muonic ^{208}Pb are presented in Table 5.4. The FNS energies denote solutions to the Dirac equation incorporating the finite nuclear size (FNS) effect, where the nuclear potential is calculated from a finite-sized nuclear model, i.e. the 2pF model. The vacuum polarization (VP) correction comprises Uehling (Ue), Wichmann-Kroll (WK), Källén-Sabry (KS), muonic Uehling (μUe), and hadronic Uehling (HUe) corrections. Each of these VP contribution is discussed in detail in Chapter 4. As for self energy (SE), it is calculated following the approach in Ref. [34], and its uncertainty is estimated based on nuclear model dependence of the results. Relativistic recoil (RRecoil) correction is calculated following Ref. [36], and its uncertainty is also determined from model dependence of

the calculation. NP corrections contribute the largest uncertainty among others. It is calculated using the Skyrme nuclear model as described in Ref. [35]. The uncertainty is determined by calculating NP corrections with nine different Skyrme parametrizations. The nine parametrizations are selected to span a wide range of parameter space. As for screening (Scrn) correction, it is a relatively simple one, as discussed in Sec. 4.6.

It is noteworthy that the corrections shown in Table 5.4 are nonlinear corrections. Therefore, summing the tabulated values will not exactly reproduce the transition energies presented in Tables 5.2. The values in Table 5.4 are calculated using the first-order perturbation theory with FNS wavefunctions, for illustrative purpose. The total transition energies are not calculated perturbatively. Since each term contributing to VP correction corresponds to an effective potential, the transition energies in Tables 5.2 are calculated by including the sum of all effective potential energies to the Dirac equation. In this manner, the solutions incorporate all of the nonlinear corrections. Similarly, screening correction is treated via an effective potential. However, SE, NP, and RRecoil cannot be represented as potentials, therefore, they are linearly added to the solutions of the Dirac equation.

All the values reported in this section are the best-fit results. A detailed description of the fitting procedure is provided in the following section.

5.4 Fitting and uncertainty analysis

The binding energies and their corresponding corrections, listed in Table 5.4, can be calculated as functions of nuclear model parameters, i.e. the a and c parameters from 2pF model. The fitting procedure determines the optimal values of these parameters by reducing the difference between theoretically calculated transition energies and experimental results. In addition, the fit must also account for the uncertainties of the values included in the fit. Therefore, a quantity relating both the differences and uncertainties of the values is defined as χ^2, characterizing the goodness of fit. The best-fit values are those that yield the smallest χ^2 value.

To present a clear picture of χ^2, we begin with the simplest case, by assuming no uncertainty correlations. Under this assumption, χ^2 is defined as

$$\chi^2 = \sum_i \left(\frac{\Delta E_i}{\sigma_i} \right)^2 , \tag{5.2}$$

where ΔE_i is the difference between theoretically calculated and experimentally measured energy of the transition labeled i, and σ_i is the uncertainty corresponding to ΔE_i. Under this definition, χ^2 can be regarded as a weighted sum of squared residuals, giving greater weights to the transitions with smaller uncertainties σ_i.

If the uncertainties are correlated, the simple uncertainty σ_i must be generalized to a covariance matrix σ, whose matrix elements are defined as

$$\sigma_{ij} = \mathrm{cov}(\Delta E_i, \Delta E_j). \tag{5.3}$$

To evaluate this covariance matrix, the following properties of covariance are particularly useful:

$$\mathrm{cov}(X, X) = \sigma_X^2 \tag{5.4}$$

$$\begin{aligned}\mathrm{cov}(aX + bY, cW + dV) = {} & ac\ \mathrm{cov}(X, W) + ad\ \mathrm{cov}(X, V) \\ & + bc\ \mathrm{cov}(Y, W) + bd\ \mathrm{cov}(Y, V),\end{aligned} \tag{5.5}$$

where X, Y, W, and V are the fitted data, a, b, c, and d are real constants, and σ_X is the uncertainty of X. In our case, ΔE_i is the difference between theoretically calculated $E_{\mathrm{theo},i}$ and experimentally measured $E_{\mathrm{exp},i}$. Therefore, by combining Eqs. (5.3) and (5.5), we have

$$\sigma_{ij} = \mathrm{cov}\left(E_{\mathrm{exp},i}, E_{\mathrm{exp},j}\right) + \mathrm{cov}\left(E_{\mathrm{theo},i}, E_{\mathrm{theo},j}\right), \tag{5.6}$$

considering no correlations between theoretical and experimental values. Next, we treat experimental measurements as uncorrelated, such that

$$\mathrm{cov}\left(E_{\mathrm{exp},i}, E_{\mathrm{exp},j}\right) = \delta_{ij}\, \sigma^2_{E_{\mathrm{exp},i}}, \tag{5.7}$$

where δ_{ij} is the Kronecker delta. As for theoretical values, some of them should have correlated uncertainties, e.g. transitions $2p_{3/2}-1s_{1/2}$ and $2p_{1/2}-1s_{1/2}$, both associated with state $1s_{1/2}$, should have correlated uncertainties. Therefore, we consider transitions involving the same state have correlated theoretical uncertainties, but different states have completely independent uncertainties. Consequently, for two transitions $A \to B$ and $C \to D$, the covariance between them can be expressed as

$$\begin{aligned}\mathrm{cov}(A - B, C - D) &= \mathrm{cov}(A, C) - \mathrm{cov}(A, D) \\ &\quad - \mathrm{cov}(B, C) + \mathrm{cov}(B, D) \\ &= (\delta_{AC} - \delta_{AD})\sigma_A^2 + (\delta_{BD} - \delta_{BC})\sigma_B^2,\end{aligned} \tag{5.8}$$

where σ_A and σ_B are the uncertainties of state A and B, respectively. This equation allows us to convert the uncertainties of states into transition energies, and the uncertainties of different states are shown in parentheses in Table 5.4.

With correlated uncertainties, the definition of χ^2 generalizes into

$$\chi^2 = (\Delta E)^T \cdot \sigma^{-1} \cdot (\Delta E), \tag{5.9}$$

where ΔE is a vector with components ΔE_i, and σ^{-1} is the inverse total covariance matrix. One can verify that this definition can be reduced to Eq. (5.2), if σ is a diagonal matrix, such that the trace of σ^{-1} becomes the sum of $1/\sigma_i^2$. The fitting procedure is performed by minimizing this χ^2, and the goodness of the fit is quantified by χ^2 per degree of freedom, χ^2/DoF. In our case, we fit data associated with 9 transitions to obtain 2 nuclear model parameters, therefore, we have DoF $= (9-2) = 7$.

5.5 Discussion

We have systematically reevaluated the theoretical transition energies and their corresponding uncertainties. By performing a χ^2 fit, we obtained nuclear charge radius with a significantly improved goodness of fit, from $\chi^2/\text{DoF} = 187$ to 9.5. However, a value of 9.5 is still larger than 1, indicating a persistent disagreement between theoretical and experimental results. In this section, we discuss the potential sources of this remaining discrepancy.

Our evaluation of nuclear charge radius relies on following assumptions:

1. The experimental measurements and their corresponding uncertainties are correct.

2. The theoretical calculations have accounted for all relevant corrections.

3. The theoretical calculations and their corresponding uncertainties are correct.

4. The 2pF nuclear model is a sufficiently accurate description of the nuclear charge distribution of ^{208}Pb.

First, we believe the experimentally measured transition energies from Bergem *et al.* [9] are very likely to be reliable, but the uncertainties might be underestimated. The values of the measurements are shown in Table 5.2 and compared with other literature results. Different measurements show relatively consistent results, but their uncertainties have different magnitude, e.g. Kessler *et al.* [7] and Anderson *et al.* [37] have much larger uncertainties. If we instead adopt their large uncertainties, the discrepancy can be completely eliminated. Therefore, due to our lack of expertise on experimental measurements, we would like to call for reassessment of transition energies of muonic ^{208}Pb.

Second, the discrepancy could in principle arise from new physics beyond the standard model, which is not accounted for in our theoretical calculation of the corrections. However, it is difficult to prove or disprove the existence of new physics with

current evidences associated with ^{208}Pb nuclear charge radius. Further independent measurements or theoretical investigations are needed to verify this possibility.

Third, we consider our theoretical calculations and the estimations of uncertainties to be reliable. Most of our calculations are very consistent with the values reported by Bergem *et al.* [9], except our RRecoil and NP calculations. The calculation methodologies for these two corrections have improved considerably in recent decades. Other than the refined uncertainty analysis, the improved calculations constitute the primary reason for the better fit obtained in our work.

Parameter	2pF	defF	3pF
c (fm)	6.6409	6.6405	6.4356
a (fm)	0.5283	0.5261	0.5557
β	–	0.05	–
w	–	–	0.2314
r_{rms} (fm)	5.5062	5.5062	5.5075
χ^2	66.8	66.8	65.2
χ^2/DoF	9.5	9.5	10.9

Table 5.5: **Nuclear parameters of ^{208}Pb determined from different nuclear models.**

Last but not least, the nuclear charge radius of ^{208}Pb is determined under the assumption of a 2pF nuclear model. To examine the validity of this assumption, we repeated the entire evaluation process using alternative nuclear models, the deformed Fermi (defF) and the three-parameter Fermi (3pF) models, which are defined in Sec. 3.4 and 3.3, respectively. The results for different nuclear models are shown in Table 5.5. By introducing nuclear deformation, the defF model does not yield notable differences in either the extracted rms radius or the χ^2 compared to the 2pF model. This is expected because the deformation parameter for ^{208}Pb is very small. By promoting the 2pF to 3pF model, we obtain a slightly different rms radius and a smaller χ^2. However, since the additional nuclear parameter w decreases the number of DoF of the fit, the overall χ^2/DoF increases slightly. This model dependence analysis does not completely validate the assumption, but it shows that in the parameter space, at the vicinity of our 2pF model, there is no better solution to further improve the fit.

Additionally, we compare our results with a list of literature values of rms nuclear radius obtained historically. The values are shown in Table 5.6, determined via either electron scattering or muonic atom spectroscopy method. These results show considerable inconsistency among different studies relative to their reported uncertainties.

Source	r_{rms} (fm)				Method
Belicard 1967	5.38(3)	5.39(3)	5.42(5)	5.54	e scattering
Anderson 1969	5.4978(30)				μ atom spec.
Heisenberg 1969	5.535	5.539	5.546		e scattering
Dreher 1974	5.498(15)	5.520(23)	5.498(10)	5.514(28)	e scattering
Kessler 1975	5.5097(6)				μ atom spec.
Euteneuer 1976	5.500(24)	5.494(24)			e scattering
Euteneuer 1978	5.4927(75)	5.5032(16)			e scattering
Bergem 1988	5.5040(11)	5.5031(11)			μ atom spec.
This work	5.5062(5)				μ atom spec.

Retrieved from Ref. [7–9, 37, 39–42].

Table 5.6: **Literature values for rms nuclear charge radius of ^{208}Pb.** The multiple values from the same source are determined via different methods, e.g. different nuclear models, electron incident energies, or analysis methods. The values determined from either electron scattering or muonic atom spectroscopy method.

In addition, the uncertainties determined from muonic atom spectroscopy method are generally smaller than those from electron scattering. We think the reasons are two-fold. On one hand, muonic atoms are inherently more sensitive to nuclear size, enabling a more precise determination of rms nuclear radius, whereas the values from electron scattering depend on electron incident energy and the specific nuclear model used in the fit. On the other hand, muonic atom spectroscopy method determines uncertainties based on a given nuclear model, which might lead to an underestimation of the actual uncertainties.

5.6 Summary and outlook

We have systematically calculated all energy corrections, with non-negligible magnitudes, of muonic ^{208}Pb. Most of the corrections are calculated via model-dependent methods, except that Wichmann-Kroll and hadronic Uehling corrections are calculated with sphere nuclear models. Due to their small magnitude, model differences will have negligible impact on the Wichmann-Kroll and hadronic Uehling corrections. Combining all the corrections with the numerical calculation of the Dirac equation, we can theoretically predict the transition energies of muonic ^{208}Pb.

By fitting our theoretical values with respect to the experimentally measured transition energies from Ref. [9], we determine the rms nuclear charge radius of ^{208}Pb

as 5.5062(5) fm. Meanwhile, we significantly reduced the fine-structure anomaly of muonic ^{208}Pb, quantified by χ^2/DoF, by a factor of twenty compared to the earlier study [9]. Our radius value differs by several standard deviations from the commonly adopted reference value of 5.5012(13) fm [43]. Given the substantial reduction of the fine-structure anomaly, we propose that our result should be adopted as the updated standard for the rms nuclear charge radius of ^{208}Pb. Furthermore, the general applicability of our method is examined by Ref. [3]. in which the same method was applied to ^{90}Zr and ^{120}Sn. The two resulting rms radii show good agreement with previous studies and have smaller uncertainties.

The anomaly of muonic ^{208}Pb has been significantly suppressed, but it remains larger than the expectation. This outcome leads to two main conclusions. First, this anomaly is not likely caused by physical effects beyond the Standard Model, a view supported by Ref. [44], and a further study of Ref. [45] using our calculated results. Second, the persisting discrepancy clearly signals the need for further investigation. In our analysis, changing the 2pF nuclear model to other similar models did not yield an improved goodness of fit. Future studies can explore more nuclear models, including more exotic ones, in order to further reduce the anomaly or to exclude a potential source of the anomaly.

Although the theoretical uncertainties of the nuclear polarization corrections are now substantially smaller than previously reported values, they still constitute the largest source of uncertainty. The large uncertainties arise mainly from our insufficient understanding of nuclear states. The calculations rely on approximate methods for the nuclear ground state, while the nuclear excited states are derived from the ground state through additional approximations. Therefore, developing more robust theoretical or numerical methods for such calculations would significantly advance the study of this fine-structure anomaly of muonic ^{208}Pb.

Bibliography

[1] Zewen Sun, Igor A. Valuev, and Natalia S. Oreshkina. Nuclear deformation effects in the spectra of highly charged ions. *Phys. Rev. Res.*, 6:023327, Jun 2024.

[2] Zewen Sun, Konstantin A. Beyer, Zoia A. Mandrykina, Igor A. Valuev, Christoph H. Keitel, and Natalia S. Oreshkina. ^{208}Pb nuclear charge radius revisited: Closing the fine-structure-anomaly gap. *Phys. Rev. Lett.*, 135:163002, Oct 2025.

[3] Konstantin A. Beyer, Igor A. Valuev, Zoia A. Mandrykina, Zewen Sun, and Natalia S. Oreshkina. Relativistic recoil as a key to the fine-structure puzzle in muonic ^{90}Zr, 2025.

[4] Zoia A. Mandrykina, Zewen Sun, and Natalia S. Oreshkina. Wichmann-kroll correction in muonic atoms and hydrogen-like electronic ions: a comparative study of two methods, 2026.

[5] G.A. Rinker and J. Speth. Nuclear polarization in muonic atoms. *Nuclear Physics A*, 306(3):397–405, 1978.

[6] Y. Yamazaki, H. D. Wohlfahrt, E. B. Shera, M. V. Hoehn, and R. M. Steffen. Discrepancy between theory and experiment in nuclear polarization corrections of muonic ^{208}Pb. *Phys. Rev. Lett.*, 42:1470–1472, May 1979.

[7] D. Kessler, H. Mes, A. C. Thompson, H. L. Anderson, M. S. Dixit, C. K. Hargrove, and R. J. McKee. Muonic x rays in lead isotopes. *Phys. Rev. C*, 11:1719–1734, May 1975.

[8] H. Euteneuer, J. Friedrich, and N. Voegler. The charge-distribution differences of ^{209}Pb, ^{208,207,206,204}Pb and ^{205,203}Tl investigated by elastic electron scattering and muonic X-ray data. *Nucl. Phys. A*, 298(3):452–476, 1978.

[9] P. Bergem, G. Piller, A. Rueetschi, L. A. Schaller, L. Schellenberg, and H. Schneuwly. Nuclear polarization and charge moments of ^{208}Pb from muonic x rays. *Phys. Rev. C*, 37:2821–2833, Jun 1988.

[10] The mpmath development team. *mpmath: a Python library for arbitrary-precision floating-point arithmetic (version 1.3.0)*, 2023. `http://mpmath.org/`.

[11] V. M. Shabaev, I. I. Tupitsyn, V. A. Yerokhin, G. Plunien, and G. Soff. Dual kinetic balance approach to basis-set expansions for the dirac equation. *Phys. Rev. Lett.*, 93:130405, Sep 2004.

[12] Maen Salman and Trond Saue. Charge conjugation symmetry in the finite basis approximation of the Dirac equation. *Symmetry*, 12(7), 2020.

[13] National Nuclear Data Center. Reduced Transition Probabilities or $B(E2; 2^+ \rightarrow 0^+)$ Values. Accessed: 2025-03-18.

[14] E. A. Uehling. Polarization effects in the positron theory. *Phys. Rev.*, 48:55–63, Jul 1935.

[15] Roy Glauber, William Rarita, and Philip Schwed. Vacuum polarization effects on energy levels in μ-mesonic atoms. *Phys. Rev.*, 120:609–613, Oct 1960.

[16] R. J. McKee. μ-atomic hyperfine structure in the k, l, and m lines of u^{238} and th^{232}. *Phys. Rev.*, 180:1139–1158, Apr 1969.

[17] K.-N. Huang. Calculation of the vacuum-polarization potential. *Phys. Rev. A*, 14:1311–1318, Oct 1976.

[18] S. Klarsfeld. Analytical expressions for the evaluation of vacuum-polarization potentials in muonic atoms. *Physics Letters B*, 66(1):86–88, 1977.

[19] Eyvind H. Wichmann and Norman M. Kroll. Vacuum polarization in a strong coulomb field. *Phys. Rev.*, 101:843–859, Jan 1956.

[20] A G Fainshtein, N L Manakov, and A A Nekipelov. Vacuum polarization by a coulomb field. analytical approximation of the polarization potential. *Journal of Physics B: Atomic, Molecular and Optical Physics*, 24(3):559, Feb 1991.

[21] Vladimir A. Yerokhin. Nuclear-size correction to the lamb shift of one-electron atoms. *Phys. Rev. A*, 83:012507, Jan 2011.

[22] V. A. Zaytsev, V. A. Yerokhin, C. H. Keitel, and N. S. Oreshkina. Qed corrections in unstable vacuum, 2024.

[23] Maen Salman and Trond Saue. Calculating the many-potential vacuum polarization density of the dirac equation in the finite-basis approximation. *Phys. Rev. A*, 108:012808, Jul 2023.

[24] V. K. Ivanov, S. S. Baturin, D. A. Glazov, and A. V. Volotka. Vacuum-polarization wichmann-kroll correction in the finite-basis-set approach. *Phys. Rev. A*, 110:032815, Sep 2024.

[25] Hans Persson, Ingvar Lindgren, Sten Salomonson, and Per Sunnergren. Accurate vacuum-polarization calculations. *Phys. Rev. A*, 48:2772–2778, Oct 1993.

[26] Jonas Sommerfeldt and Paul Indelicato. All-order wichmann and kroll contribution in heavy electronic and exotic atoms, 2025.

[27] G. Källén and A. Sabry. Fourth Order Vacuum Polarization. *Dan. Mat. Fys. Medd.*, 29(17):1–20, 1955.

[28] J. Blomqvist. Vacuum polarization in exotic atoms. *Nuclear Physics B*, 48(1):95–103, 1972.

[29] L. Wayne Fullerton and G. A. Rinker. Accurate and efficient methods for the evaluation of vacuum-polarization potentials of order $z\alpha$ and $z\alpha^2$. *Phys. Rev. A*, 13:1283–1287, Mar 1976.

[30] P. Indelicato. Nonperturbative evaluation of some qed contributions to the muonic hydrogen $n = 2$ lamb shift and hyperfine structure. *Phys. Rev. A*, 87:022501, Feb 2013.

[31] S. Breidenbach, E. Dizer, H. Cakir, and Z. Harman. Hadronic vacuum polarization correction to atomic energy levels. *Phys. Rev. A*, 106:042805, Oct 2022.

[32] V. A. Yerokhin and V. M. Shabaev. First-order self-energy correction in hydrogenlike systems. *Phys. Rev. A*, 60:800–811, Aug 1999.

[33] Natalia S. Oreshkina, Halil Cakir, Bastian Sikora, Vladimir A. Yerokhin, Vincent Debierre, Zoltán Harman, and Christoph H. Keitel. Self-energy-corrected dirac wave functions for advanced qed calculations in highly charged ions. *Phys. Rev. A*, 101:032511, Mar 2020.

[34] Natalia S. Oreshkina. Self-energy correction to the energy levels of heavy muonic atoms. *Phys. Rev. Res.*, 4:L042040, Nov 2022.

[35] Igor A. Valuev, Gianluca Colò, Xavier Roca-Maza, Christoph H. Keitel, and Natalia S. Oreshkina. Evidence against nuclear polarization as source of fine-structure anomalies in muonic atoms. *Phys. Rev. Lett.*, 128:203001, May 2022.

[36] Vladimir A. Yerokhin and Natalia S. Oreshkina. Qed calculations of the nuclear recoil effect in muonic atoms. *Phys. Rev. A*, 108:052824, Nov 2023.

[37] H. L. Anderson, C. K. Hargrove, E. P. Hincks, J. D. McAndrew, R. J. McKee, R. D. Barton, and D. Kessler. Precise measurement of the muonic x rays in the lead isotopes. *Phys. Rev.*, 187:1565–1596, Nov 1969.

[38] M. V. Hoehn and E. B. Shera. Energies of the muonic l and m transitions of the even-a pb isotopes. *Phys. Rev. C*, 30:704–708, Aug 1984.

[39] J. B. Bellicard and K. J. van Oostrum. Elastic electron scattering from Lead-208 at 175 and 250 MeV. *Phys. Rev. Lett.*, 19:242–244, Jul 1967.

[40] J. Heisenberg, R. Hofstadter, J. S. McCarthy, I. Sick, B. C. Clark, R. Herman, and D. G. Ravenhall. Elastic electron scattering by Pb^{208} and new information about the nuclear charge distribution. *Phys. Rev. Lett.*, 23:1402–1405, Dec 1969.

[41] B. Dreher, J. Friedrich, K. Merle, H. Rothhaas, and G. Lührs. The determination of the nuclear ground state and transition charge density from measured electron scattering data. *Nucl. Phys. A*, 235(1):219–248, 1974.

[42] H. Euteneuer, J. Friedrich, and N. Voegler. Charge distribution of ^{208}Pb and the difference in $\rho(r)$ for Pb and Tl investigated by by elastic electron scattering. *Phys. Rev. Lett.*, 36:129–132, Jan 1976.

[43] I. Angeli and K.P. Marinova. Table of experimental nuclear ground state charge radii: An update. *Atomic Data and Nuclear Data Tables*, 99(1):69–95, 2013.

[44] K.A. Beyer, I.A. Valuev, C.H. Keitel, M. Tamburini, and N.S. Oreshkina. Challenging beyond-the-standard-model solutions to the fine-structure anomaly in heavy muonic atoms. *Physics Letters B*, 854:138746, 2024.

[45] K. A. Beyer and N. S. Oreshkina. Self-consistent bounds on beyond the standard model bosons from spectroscopy of muonic atoms with magic nuclei, 2025.